ChemElectroChem

Review
doi.org/10.1002/celc.202400648

Chemistry Europe
European Chemical Societies Publishing

www.chemelectrochem.org

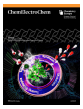

Perovskite Oxides for Electrocatalytic Hydrogen/Oxygen Evolution Reaction

Lu Lu,[a, b] Mingzi Sun,[a, b] Tong Wu,[a, b] Qiuyang Lu,[a, b] Baian Chen,[a, b] Cheuk Hei Chan,[b] Hon Ho Wong,[b] Zikang Li,[a, b] and Bolong Huang*[a, b]

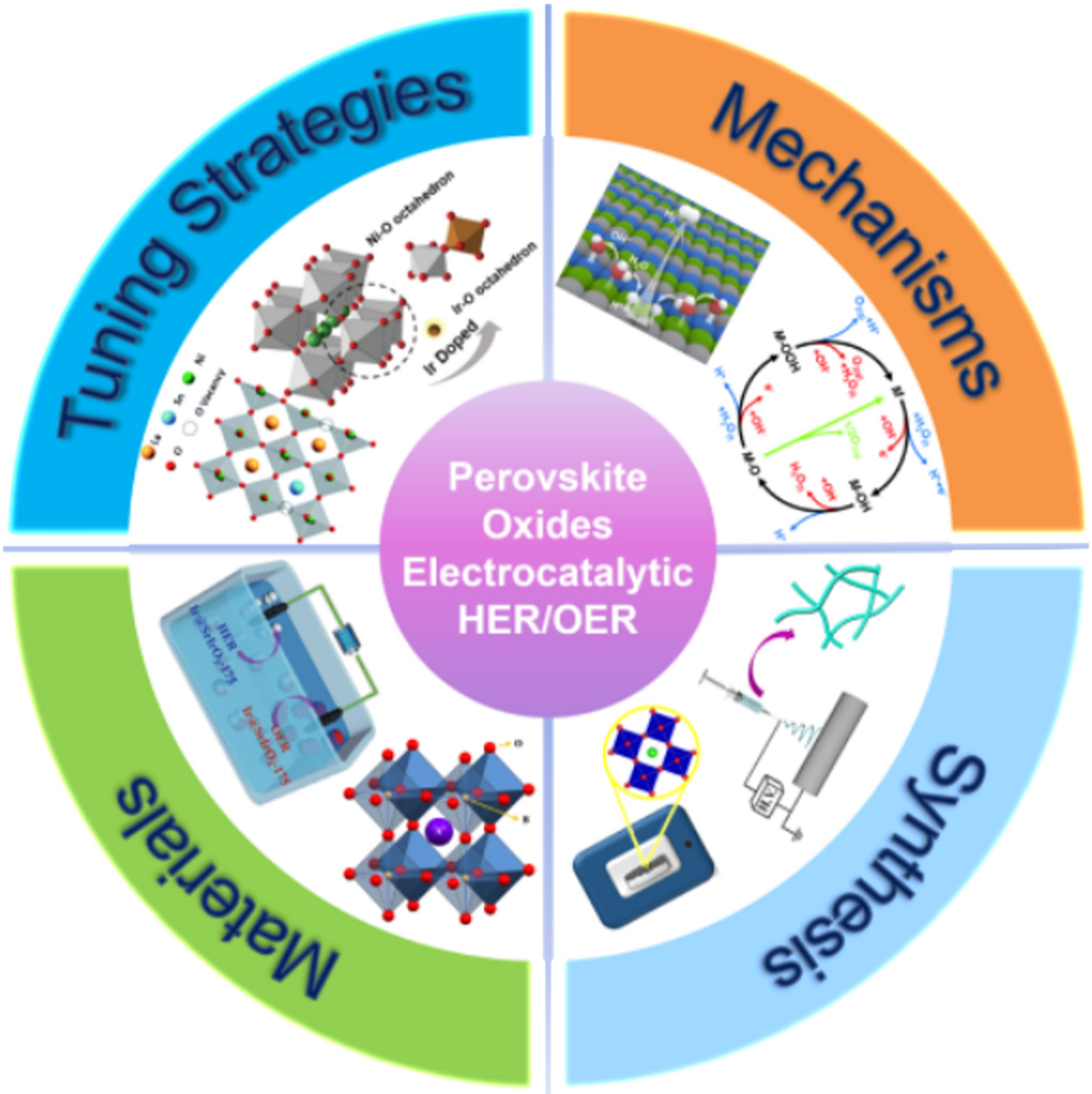

Since the excessive exploitation of fossil fuels will cause wars for oil, developing sustainable and eco-friendly energy resources to solve the energy crisis and realize the carbon-neutrality goal has been a hot issue. Water electrolysis has been acknowledged as a promising technology for hydrogen (H_2)/oxygen (O_2) evolution reaction (HER/OER) since the overall water splitting reaction rates can be well controlled by applying appropriate electrode voltage. Whereas the sluggish electrochemical reactions kinetics on both the cathode and anode have greatly restricted the energy conversion efficiency. Thus, developing highly active electrocatalysts to reduce the overpotentials required for electrolytic HER/OER is of great significance in increasing the utilization rates of electrical power and lowering production costs. ABO_3-structured perovskite-oxides based electrocatalysts possess the merits of low cost, high structural stability, and lattice compatibility, and thus they have attracted intense research attention in recent decays. To inspire both theoretical and experimental researchers to design novel perovskite-oxide electrocatalysts for efficient HER/OER, the fundamental electrode reaction mechanisms, the effects of synthetic methods on material morphologies, recently reported perovskite-oxide electrocatalysts and effective tuning strategies on enhancing the electrocatalytic activities of existing perovskite-oxides have been fully discussed in this review.

1. Introduction

Nowadays, the excessive exploitation and consumption of conventional fossil fuels like petroleum, natural gas, as well as coal, have brought about severe energy crises and environmental risks.[1] Thus, it is significant to explore renewable and eco-friendly energy resources for the achieving of carbon-neutrality goals. Hydrogen (H_2) has a high calorific value of 282 kJ/mol, and the combustion product is only water (H_2O), causing zero pollution.[2] H_2 has been treated as a promising energy carrier since zero carbon emission will be caused in the energy cycle of water-splitting H_2 evolution and combustion.[1] In terms of environmental protection and carbon neutrality, producing H_2 via the electrolysis of water exhibits its superiority over industrialized technologies that are based on the cracking of fossil fuels. However, caused by the large overpotential, a relatively high voltage (1.80 V–2.40 V) is demanded to reach enough current density (200 mA/cm^2–400 mA/cm^2), which is much higher than the theoretical thermodynamic minimum voltage of 1.23 V.[3] Consequently, huge consumption in electricity power still cannot be avoided in the current water electrolysis-based H_2 production industry. The overall water-splitting efficiency depends on the cathodic hydrogen evolution reaction (HER) and anodic oxygen (O_2) evolution reaction (OER). HER involves a two-electron process ($2H_2O + 2e^- \rightarrow H_2 + 2OH^-$) while OER involves a four-electron process ($4OH^- \rightarrow O_2 + 2H_2O + 4e^-$). To reduce the overpotential and further accelerate the corresponding electrode reaction rate, finding highly active electrocatalysts to lower the energy barrier has become a recent research hotspot.

For electrocatalytic HER, Pt-based materials are generally regarded as the benchmark electrocatalysts, while for OER, noble-metal based materials including Pt/C, RuO_2, and IrO_2 are the most popular catalysts.[3,4] But in fact, limited by the high cost and scarcity of resources, noble metals based electrode materials have not been largely applied in industrial productions. It is imperative to exploit low-cost but high-efficiency catalysts for the large-scale production of H_2/O_2 through water electrolysis. Simple non-noble transition metal (TM) oxides based electrocatalysts have attracted much research attention since they have high material durability and lattice compatibility. They have limited active TM sites on the material surface for the efficient adsorption of reactants and intermediates, thus resulting in a relatively low catalytic activity. With active heteroatoms doped, both the electron transfer and molecular adsorption can be improved at the catalytic centers.[5] Through surface modification or interface engineering, non-noble TM heterostructures based catalysts such as (Ni, Fe)S_2@MoS_2,[6] Co_9S_8/Ni_3S_2,[7] and $Ni(OH)_2/Ni_3S_2$[8] are also potential alternatives for water splitting. TMs based single atom catalysts (SACs) also exhibit their merits for surface reactions due to their high atomic utilization rate and isolated active sites on catalytic surfaces for efficient molecular adsorption,[9] but the structural stability of SACs still needs to be further improved.

Compared to SACs, perovskite oxides based catalysts exhibit their unique advantages of low cost, high structural stability and lattice compatibility, easy to synthesize, as well as tunable electronic properties.[1,10] Perovskite oxides are commonly built in the ABO_3 structure, in which the A-sites are generally formed by rare-earth (RE), alkaline-earth, or alkali metals with twelve coordinated O-atoms, while B-sites are constituted by TMs with six coordinated O-atoms (Figure 1a–b[11]). The A-/B- sites or O-sites can be occupied by a series of selected elements from the periodic table, resulting in a regulated electronic structure. When partially doped/substituted by external atoms, their high lattice stability can still be kept with controllable valence states and O-vacancies created.[12] The broad regulation range of the nonstoichiometric ratio at O sites is beneficial to the modulation of electronic properties and thus facilitates the electron transfer process.[13] Though equipped with excellent adjustability and durability, the electrocatalytic HER/OER activity of single-phase perovskite oxides still cannot satisfy the requirements of large-scale industrial production because of their low native conductivity and limited surface active sites.[11] Researchers hence attempt to improve the electrocatalytic activity of

[a] L. Lu, M. Sun, T. Wu, Q. Lu, B. Chen, Z. Li, B. Huang
Department of Chemistry, City University of Hong Kong, Kowloon, Hong Kong SAR, China
E-mail: b.h@cityu.edu.hk
[b] L. Lu, M. Sun, T. Wu, Q. Lu, B. Chen, C. Hei Chan, H. Ho Wong, Z. Li, B. Huang
Department of Applied Biology and Chemical Technology, The Hong Kong Polytechnic University, Hung Hom, Kowloon, Hong Kong SAR, China

perovskite oxides through various methods including surface/interface engineering,[14] heteroatoms doping,[15] defects engineering,[16] as well as morphological/dimension controlling.[17]

The changeable oxidation states of transition metal elements in perovskite-oxide lattices are beneficial for electronic structure regulations through external doping.[18] By defects engineering, the mobility of charge carriers, the production of redox couples, as well as the kinetics of O-exchange in perovskite-oxide electrocatalysts can be remarkably promoted.[18–19] For instance, perovskite-oxide $Ba_{0.5}Sr_{0.5}Co_{0.8}Fe_{0.2}O_{3-\delta}$ has already been reported as a potential bifunctional electrocatalyst for both HER[20] and OER.[21] The adjustable electronic properties of perovskite-oxides enable the investigations of the relationships between electronic structures and catalytic activities in electrocatalytic reactions.[22] The non-stoichiometric structural characteristics of ABO_3 perovskites largely affect the 3d-σ* antibonding orbitals of transition metals. The variations in electron occupation status can alter the spin states and further affect the bonding between metals and oxygens, leading to the shifting in d-band positions and O-p orbitals.[22,23] The manufacturing of nanoscale perovskite-oxide electrocatalysts is also a valid technique to improve the catalytic activity for overall electrocatalytic water splitting.[24] Especially, the emerging electrospinning technique greatly facilitates the large-scale synthesis of one-dimensional highly porous nanoscale perovskite-oxides with high specific surface areas, including nanotubes, nanorods, as well as nanofibers.[24,25] Under reducing ambiance, the exsolution of B-site metals will make the metal atoms well dispersed on the material surface, resulting in an improved surface exchange efficiency as well as synergetic effects for bifunctional electrocatalysis.[26]

To provide a reference for the developments of novel perovskite oxides based electrocatalysts for efficient HER/OER, the mechanisms, synthetic methods, tuning strategies, and explanations of material properties by density functional theory (DFT) calculations are the main focuses in this review. In addition, the challenges to the industrialization of perovskite oxides based electrocatalysts will also be discussed in the work.

Dr. Bolong Huang is a Professor at the Department of Chemistry of City University of Hong Kong. His main research fields are electronic structures of nanomaterials, energy materials, solid functional materials, and rare earth materials, as well as their applications in multi-scale energy conversion and supply systems. Dr. Huang has published 339 research papers and has received citations over 27000 times with h-index of 94. He is the Associate Editor of Battery Energy and Frontiers in Chemistry, the Early Career Advisory Board of JACS Au, and the Young Star Editor of Nano Research.

2. Mechanisms of Water Splitting

The overall water splitting reaction is composed of two simultaneous half-reactions, cathodic HER and anodic OER.[27] Having a deep insight into the fundamental reaction mechanisms of HER and OER will direct the confirmation of the rate-determining step (RDS) and give theoretical references for the design and tuning of candidate electrocatalysts. Water electrolysis can be conducted within a broad pH range by the following overall reaction equation:

$$2H_2O \rightarrow 2H_2 + O_2 \quad (1)$$

With the reference to a standard hydrogen electrode (SHE), when pH = 0, with the combination of proton-electron (H^+-e^-) pairs, HER will proceed at the cathode by the following formula:

$$4H^+ + 4e^- \rightarrow 2H_2,\ E^{Cathode} = 0\ V \quad (2)$$

Simultaneously, O_2 will be generated by the oxidization of H_2O molecules at the anode via the formula indicated below:

$$2H_2O \rightarrow O_2 + 4H^+ + 4e^-,\ E^{Anode} = 1.23\ V \quad (3)$$

While pH = 14, the two half-reactions (HER and OER) will take place at the cathode and anode respectively as the two formulas indicated as follows:

$$4H_2O + 4e^- \rightarrow 4OH^- + 2H_2,\ E^{Cathode} = -0.83\ V \quad (4)$$

$$4OH^- \rightarrow O_2 + 2H_2O + 4e^-,\ E^{Anode} = 0.40\ V \quad (5)$$

The differences in the source of adsorbed hydrogen (H*) under acidic and alkaline conditions will give rise to the differences in the RDS and surface reaction paths. Theoretically, an electric potential of 1.23 V (298 K, 1 atm) is needed to induce HER/OER, but in fact, additional overpotential is required to guarantee the electrolytic reaction takes place at an adequate reaction rate. Thus, exploring novel electrocatalysts to lower the overpotential of HER/OER has always been a hot topic in the field of new energy.

2.1. HER Mechanisms

HER involves a two-electron transfer process while OER proceeds with a four-electron transfer process. Theoretically, electrocatalytic HER occurs more easily than OER. As illustrated in Figure 2a,[28] two different reaction paths have been generally adopted to describe the HER mechanisms, that is, the Volmer-Heyrovsky step or the Volmer-Tafel step.[29] The surface coverage rate of H* decides which step serves as the dominant HER mechanism. The reaction will dominantly proceed through the Volmer – Heyrovsky path under a low H* coverage rate, while under a high H* coverage, the HER will take place faster by the Volmer – Tafel path.[11]

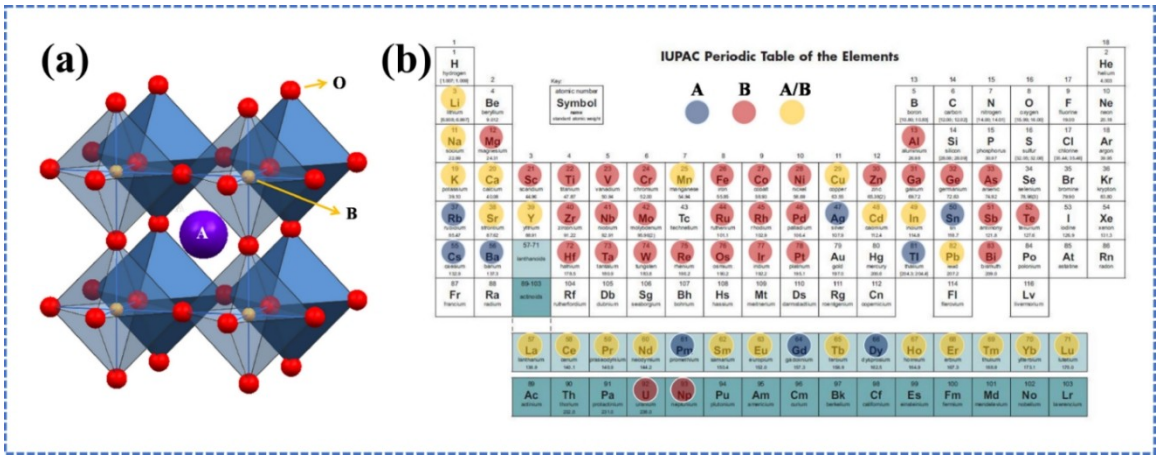

Figure 1. (a) Schematic depiction for typical ABO_3-structured perovskite oxides; (b) The frequently-applied metal elements at the A-sites or B-sites in perovskite-oxide lattice.[11] Copyright 2022, Multidisciplinary Digital Publishing Institute.

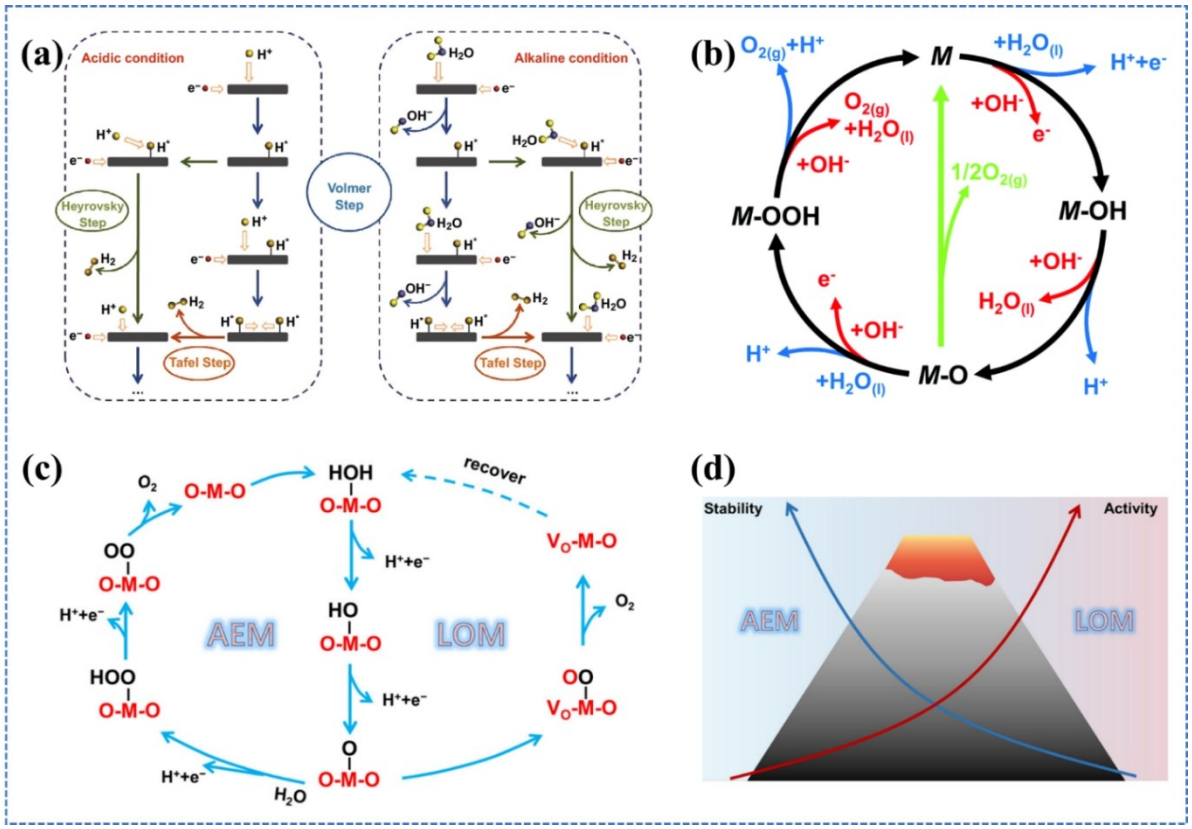

Figure 2. (a) Schematic HER mechanisms by Volmer-step (blue), Heyrovsky-step (yellow-green), as well as Tafel-step (Orange) in acidic (left) and alkaline media (right), respectively.[28] Copyright 2018, Springer Nature. (b) Schematic OER mechanisms in acidic (red) and alkaline (blue) media respectively with the reaction routes by OOH* (black) or two O* combining together (green).[35] Copyright 2017, Royal Society of Chemistry. (c) The illustration of OER routes by AEM (left) and LOM (right), respectively; (d) the competitive relationships between stability and activity for AEM and LOM.[34b] Copyright 2023, Wiley-VCH.

2.1.1. Under Acidic Conditions

In acidic conditions, with the introduction of one e^-, the intermediate products H* are mainly generated from the direct adsorption of abundant H^+ in solution, see Equation (6). With the continuous participation of H^+ and e^-, H_2 will be created by the Heyrovsky step, which is the RDS as Equation (7) indicated. The evolution of H_2 will proceed faster by the direct combination of two adjacent H* by the Tafel step as Equation (8) illustrated when the coverage rate of H* is high enough on the catalytic surface.[30]

$$\text{Volmer reaction}: \quad H^+ + * + e^- \rightarrow H^* \tag{6}$$

$$\text{Heyrovsky reaction}: \ H^+ + H^* + e^- \rightarrow^* + H_2 \quad (7)$$

$$\text{or Tafel reaction}: \ 2H^* \rightarrow 2^* + H_2 \quad (8)$$

2.1.2. Under Neutral/Alkaline Conditions

In neutral/alkaline conditions, as Equation (9) indicated, the intermediates H* are mainly from the splitting of H_2O molecules since the quantity of H^+ at the solid-liquid interface is not adequate to drive the direct adsorption reaction. Different from the situations in acidic conditions, the Volmer step is the RDS, and thus the H_2O adsorption (H_2O_{ad}) strength at active sites together with the following water splitting rate will be the main influence factors for the HER efficiency. To guarantee the subsequent H_2 evolution rate, in the Heyrovsky step of Equation (10), the faster desorption of OH* is also important for the release of active sites. If the reaction rates of water splitting and the removal of OH* are fast enough to create a catalytic surface rich in H*, the following H_2 evolution process will occur via the Tafel step, as indicated in Equation (11).

$$\text{Volmer reaction}: \ H_2O + {}^* + e^- \rightarrow H^* + OH^- \quad (9)$$

$$\text{Heyrovsky reaction}: \ H_2O + H^* + e^- \rightarrow^* + OH^- + H_2 \quad (10)$$

$$\text{or Tafel reaction}: \ 2H^* \rightarrow 2^* + H_2 \quad (11)$$

2.2. OER Mechanisms

Compared to two-electron transfer HER, the reaction mechanisms of four-electron transfer OER are more complex. The slow kinetics of OER limit the reaction rate of water electrolysis, therefore it has been treated as the main obstacle to the improvement of energy-conversion efficiency in overall water-splitting reaction.[31] In acidic solution, the occurrence of OER is highly dependent on pH variation, and the O_2 molecules are mainly produced from the oxidization of H_2O, along with the creation of H^+-e^- pairs.[32] In alkaline solution, the O_2 molecules are generated from the oxidization of hydroxyl ions (OH^-), accompanied by the formation of H_2O molecules and the liberation of e^-.[33] Based on the features of catalytic/adsorption active sites revealed by DFT simulations, the OER mechanisms can be explained by the adsorbate evolution mechanism (AEM, proposed by Nørskov) or lattice oxygen mechanism (LOM).[2,34] The AEMs in both acidic and alkaline conditions have been illustrated in Figure 2b.[35]

2.2.1. AEM in Acidic Conditions

The general mechanism of OER in acidic conditions has been demonstrated in Figure 2b[35] by the catalytic cycle labeled in red color. In the first step, the H_2O molecules are aggregated and then adsorbed at the catalyst surface and followed by two de-protonation reactions as indicated in formula (12–13), intermediates O* are obtained at adsorption sites. Then, the intermediate products OOH* will be formed by the nucleophilic collisions of H_2O molecules, see formula (14). In the last step, the O_2 molecules are generated from OOH* through another de-protonation reaction, and the desorption of O_2 will recover the catalyst surfaces for the next catalytic reaction cycles, as illustrated in formula (15).

$$^* + H_2O \rightarrow H^+ + OH^* + e^- \quad (12)$$

$$OH^* \rightarrow H^+ + O^* + e^- \quad (13)$$

$$O^* + H_2O \rightarrow H^+ + OOH^* + e^- \quad (14)$$

$$OOH^* \rightarrow H^+ + {}^* + O_2 + e^- \quad (15)$$

2.2.2. AEM in Neutral/Alkaline Conditions

In Figure 2b,[35] as the catalytic cycle labeled in blue color indicated, the basic mechanism of OER in an alkaline solution involves four-step oxidation processes, with the participation of OH^-. Firstly, OH^- are captured and adsorbed at active sites on catalyst surfaces, and the adsorption intermediates OH* will transformed into O* by the following de-protonation reaction, see Equation (16–17). Subsequently, with the collision of another OH^- to O*, the crucial intermediates OOH* will be created, see Equation (18). As indicated in Equation (19), by the de-protonation of OOH*, the O_2* structures will be produced and finally the O_2 molecules will be released from the active sites for the regeneration of the catalytic surface.

$$OH^- + {}^* \rightarrow OH^* + e^- \quad (16)$$

$$OH^- + OH^* \rightarrow H_2O + O^* + e^- \quad (17)$$

$$OH^- + O^* \rightarrow OOH^* + e^- \quad (18)$$

$$OH^- + OOH^* \rightarrow H_2O + {}^* + O_2 + e^- \quad (19)$$

2.1.3. LOM

The LOM controlled OER involves the bonding of lattice oxygen (O_L) to O* or the direct oxidation of two O_L atoms (Figure 2c[34b]). It has been verified in previous studies that both the compositions and lattice structures of electrocatalysts suffer obvious variations in OER.[36] The results of the isotopic labeling method and differential-electrochemical mass spectrometry revealed that the origin of O_2 created by surface catalytic reactions is partly from the O-atoms in the catalyst lattice.[37] Like AEM in acidic conditions, the crucial intermediates O* in LOM can be obtained by two consecutive de-protonations of H_2O*, see Equations (12)-(13). The bonding of intermediate

adsorbates O* and O_L atoms will cause the creation of O_2 molecules and oxygen-vacancy (V_O) defects, see Equation (20), or O_2 molecules can be produced from the direct bonding of two O_L atoms, see Equation (21).[38] The V_O defects that are generated from the losses of O_L atoms can be refilled by the O-atoms from de-protonated H_2O molecules, along with the formation of H* and H^+, see Equation (22).[39] The surface active sites will be recovered for the next catalytic cycle after the desorption of H*, see Equation (23).

$$O_L + O^* \rightarrow V_O + O_2 \quad (20)$$

$$2O_L \rightarrow 2V_O + O_2 \quad (21)$$

$$H_2O + V_O \rightarrow H^+ + H^* + O_L + e^- \quad (22)$$

$$H^* \rightarrow H^+ + * + e^- \quad (23)$$

Actually, the AEM and LOM occur simultaneously with a competitive relationship, see Figure 2d.[34b] Because of the direct coupling between O-atoms in the host lattice to the O-atoms contained in adsorbed intermediates such as OH* and OO*, the kinetic barriers and theoretical voltages of LOM are relatively lower than those of AEM, and hence the LOM dominated OER usually exhibits a higher electrocatalytic activity.[11,40] The intrinsic lattice structures in AEM will remain stable since reactions mainly involve the surface adsorbed intermediates (OH*, O*, OOH*, OO*), while the depletion of lattice O-atoms in LOM will cause dynamic structure changes in perovskite-oxides lattices.[41] LOM not only causes the creation of V_O defects but also speeds up the dissolution rate of metal atoms, inducing lattice collapse and thus bringing about fast de-activation of perovskite-oxide catalysts.[42]

3. Synthesis of Perovskite Oxides

A series of synthetic methods have been employed for the fabrication of perovskite-oxides based electrocatalysts, such as traditional solid-state methods,[43] precipitation methods,[44] combustion,[45] and hydrothermal/solvothermal synthesis,[46] electrospinning,[47] sol-gel[48] and polymer-assisted deposition (PAD).[49] Some conventional approaches, like solid-sate synthesis, precipitation methods, as well as combustion synthesis, must be conducted with specific devices under high-temperature/high-pressure condition. The reaction products as prepared under harsh conditions are usually on the micrometer scale, resulting in a limited specific surface area for electrocatalytic reactions. By hydrothermal/solvothermal approach, the product morphology can be well controlled, but limited by the volume of autoclave reactors, large-scale production cannot be achieved. With simple treatments like calcination and heat treatment, an improved productivity of perovskite oxides can be obtained by sol-gel and polymer-assisted synthesis.[50] Besides, with subsequent de-alloying treatment, a novel synthetic strategy by directly transforming bulk pristine alloy materials into a series of nanoscale porous perovskite $LaMO_3$ (M = Cr, Mn, Co, or Ni) has been reported.[51] Through this facile synthesis protocol, a nanoporous perovskite $LaMO_3$ can be generated with a high surface-to-bulk ratio and high stability, exhibiting bifunctional catalytic activities toward both OER and oxygen reduction reaction (ORR) in alkaline media with methanol-resistance property.[51]

3.1. Conventional Solid-State Synthesis

Perovskite oxides can be conventionally prepared by transforming more than two kinds of metal-oxide reactants into one compound product via calcination processing. The solid-state reaction synthesis has a simple flow, and it is eco-friendly without the emission of poisonous gaseous products. Nonetheless, harsh conditions especially high-temperature condition are essential for the proceeding of solid-state reaction, and the as-obtained final products usually suffer from large particle size, resulting in a relatively limited specific surface area that restrains the efficient utilization of surface active sites.[50] In addition, impurities/defects will appear in the perovskite-oxide lattice owing to the inadequate mixing of metal-oxide precursors, causing a decline in electrocatalytic activity. Thus, the perovskite oxides prepared by solid-state reactions have been previously applied in the investigations of charge transport mechanisms, electronic properties, or magnetic properties.[43,52] A typical perovskite-oxide compound $LaCo_{1-x}Ni_xO_3$ has been fabricated by combining three simple types of metal oxides (La_2O_3, Co_2O_3, as well as NiO) at a specific stoichiometric ratio by heat treatment at a high temperature of 900 °C and then 1200 °C under air ambiance.[43] As indicated in Figure 3a,[53] $RuNiO_3$ is another recent example of solid-state method prepared perovskite oxides. Two metal oxides (RuO_2 and NiO) were grinded into powder at a certain stoichiometric ratio, and then heated to 850 °C with a temperature gradient of 3.0 °C/min. After heating for 4 hours, the fine-powder $RuNiO_3$ can be obtained by a natural cooling-down treatment to 25 °C as well as a subsequent grinding process. The $RuNiO_3$ nanoparticles modified Ni-foam electrocatalyst has high activity at high electric current densities and a relatively low potential of 0.8 V with reference to Hg | HgO electrode.[53]

3.2. Hydrothermal/Solvothermal Methods

Harsh reaction conditions such as High-temperature and high-pressure are usually required in hydrothermal/solvothermal crystallization, and for the preparation of perovskite oxides, an additional post-annealing process is needed. However, in comparison with the high calcining temperature in the sol-gel technique, the temperature required in the annealing process has been remarkably diminished by hundreds of degrees centigrade.[54] A novel porous-hollow $LaNiO_3$/N,S-graphene compound has been prepared by hydrothermal method.[46b] The graphene-oxide precursor has been prepared by a modified Hummer's approach, and the N, S-modified product can be obtained by the following sonicating and dispersing treatments

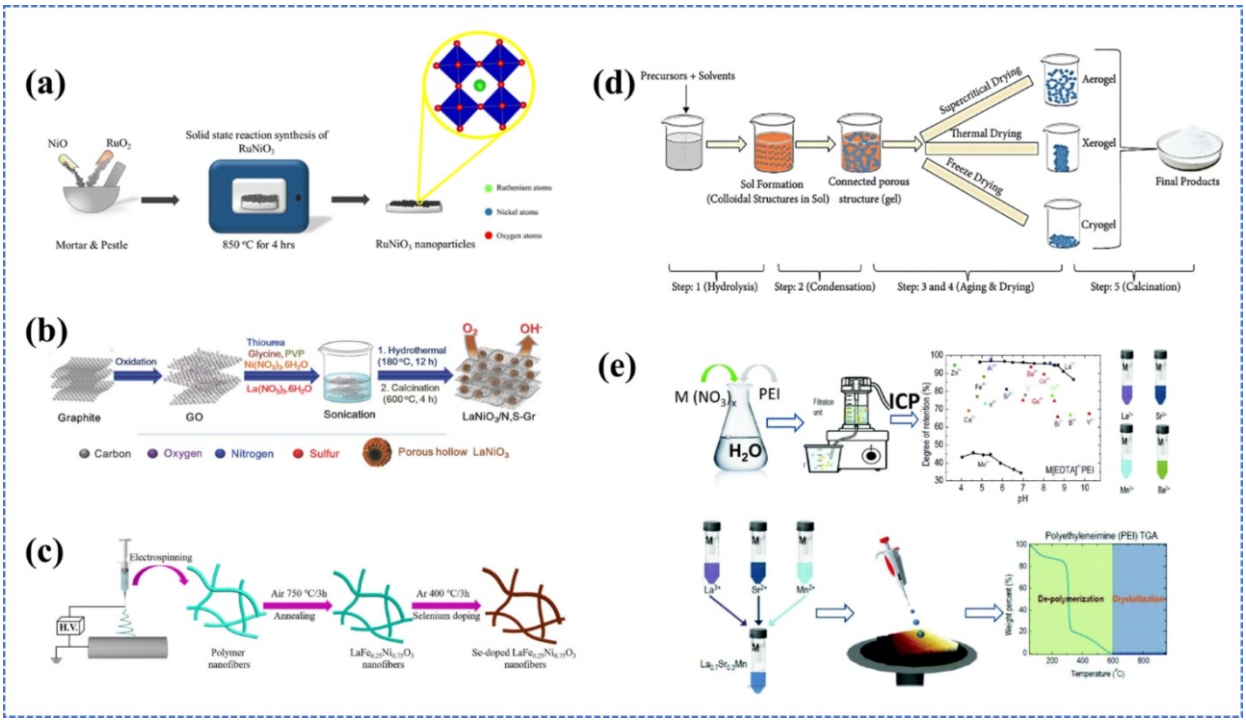

Figure 3. (a) The diagram of typical solid-state synthesis for perovskite-oxide $RuNiO_3$.[53] Copyright 2023, Royal Society of Chemistry. (b) The schematic depiction of a novel $LaNiO_3$/N,S-graphene nano-material assembled by hydrothermal synthesis.[46b] Copyright 2017, Wiley-VCH. (c) Schematic fabrication of a novel $LaFe_{0.25}Ni_{0.75}O_3$: Se nanofiber by electrospinning.[57d] Copyright 2020, American Chemical Society. (d) Schematic illustration of the main steps involved in sol-gel technique: from precursors to aerogel and final solid-sate products.[58] Copyright 2021, Wiley-VCH. (e) The illustration of the main stages involved in PAD.[61] Copyright 2018, Royal Society of Chemistry.

with thiourea in ultra-pure water. Subsequently, the as-obtained solution will be mixed with precursors $La(NO_3)_3$ and $Ni(NO_3)_2$, glycine, as well as poly-vinylpyrrolidone. The homogeneous aqueous solution will be further transferred into an autoclave to conduct the following hydrothermal reaction (180 °C, 12 hours). The as-prepared mixture will be thoroughly washed, dried, and finally annealed at a temperature of 600 °C in Ar-gas environment to get the perovskite-oxides/N,S-graphene composite material (Figure 3b[46b]).

3.3. Electrospinning

Though many perovskite-oxides have bifunctional electrocatalytic activities (OER and ORR) under alkaline condition, the limited surface-volume ratio of the perovskite-oxides produced via conventional high-temperature approaches will reduce the material utilization rate. The electrospinning technique is mild and low-cost, and it has been widely used for the synthesis of nanoscale perovskite oxides based electrocatalysts in diverse morphologies, including nanotubes,[55] nanorods,[56] as well as nanofibers[57] (Figure 3c[57d]). With subsequent annealing treatment, a mesoporous perovskite-oxide $La_{0.5}Sr_{0.5}CoO_{3-x}$ nanotube has been prepared by electrospinning, and it still maintains bifunctional electrocatalytic activities with high cycling durability under a testing current density of 0.1 mA/cm^2.[55a] By electrospinning and composition/morphology rationalization, a nano-hybrid formed by perovskite-oxide $La_{0.5}(Ba_{0.4}Sr_{0.4}Ca_{0.2})_{0.5}Co_{0.8}Fe_{0.2}O_{3-\delta}$ nanorod and reduced graphene-oxides (rGOs) nanosheet has been developed to serve as a bifunctional electrode under alkaline condition.[56a] Integrated with calcination processing, a lanthanum-based perovskite-oxide nanofiber $LaNi_{0.85}Mg_{0.15}O_3$ that exhibits bifunctional catalytic activities has been synthesized via electrospinning technology.[57a] In comparison with precursor $LaNiO_3$ nanofibers, the half-wave potential of the electro-spun $LaNi_{0.85}Mg_{0.15}O_3$ has been increased to 0.69 V and the overpotential has been diminished to 0.45 V under the electric current density of 10 mA/cm^2.[57a]

3.4. Sol-Gel Synthesis

The sol-gel synthesis is a versatile approach for the fabrication of perovskite oxides by the inorganic polymerization reaction of metal precursors such as metal-nitrates/acetates. In comparison with solid-state synthesis, it exhibits the advantages of a purer phase-structure and milder reaction conditions. The main processes in general sol-gel synthesis have been indicated in Figure 3d.[58] The key point of the sol-gel method is the precise composition control of the molecular precursors with optimized reaction conditions kept for the transformation from a colloidal solution to a solid-state product via a transitional gel state.[59] The material morphology, composition, and phase-structure can be precisely controlled through the sol-gel method to satisfy the requirements in different application scenarios.

Firstly, controlled in appropriate stoichiometric ratios, the precursors will be dissolved, thoroughly mixed, and then added with chelating agents like ethylene-diamine-tetraacetic-acid (EDTA), and binding agents like ethylene-glycol if needed. With the addition of NH_4OH solution, the pH can be regulated in the range of 6–8 to guarantee the thorough chelation of metal precursors and chelating agents. After a thorough stirring and then an evaporating treatment at 100 °C, the as-prepared mixture will transform into a gel state. A fluffy product can be obtained after heating at 300 °C, and after calcination in a specific gaseous environment such as the Ar-atmosphere, the solid-state product that can serve as an electrocatalyst will be obtained.[60]

3.5. Polymer-Assisted Deposition

The physical/chemical properties of as-prepared metal-polymer complex solutions have great impacts on the film-growth quality of precursors. Like the typical chemical solution deposition (CSD) technique, the growth of precursor thin films has also been treated as the key procedure of PAD, including solution preparation, coating, as well as heat treatment (Figure 3e[61]). Nevertheless, the chemicals applied in the preparation of metal-polymer complex precursor solutions in PAD are different from those in typical CSD techniques.[49] Since the viscosity of solutions affects the coating quality of thin films to a great extent, high stability and high homogeneity are essential to the as-prepared precursor solutions. Hence, water-soluble polymers are added to coordinate with the metal ions and further stabilize them by hydrogen/covalent bonding or electrostatic-attraction effects.[49,62] Since it was first reported in 2004,[63] the polymer-assisted approach has been widely applied for the manufacturing of functional epitaxial composite materials and multi-layer thin perovskite films with a thickness of less than 100 nm. Combined with crystallization treatment via rapid thermal annealing (RTA), highly active epitaxial double-perovskite thin-film materials, La_2CoMnO_6 as well as La_2NiMnO_6, have been successfully fabricated by PAD processing.[64] To demonstrate the key characteristics of the synthetic methods discussed above, their main advantages and limitations have been summarized in **Table 1**.

4. Perovskite Oxides Based Electrocatalysts

4.1. Perovskite Oxides for HER

For single-active site catalysts-based HER, the H_{ad} and H-desorption will occur at the same adsorption site, and hence it passes through a short-distance/non-interface reaction route for in-situ catalytic reaction but usually suffers a high energy barrier for H-desorption (Figure 4a[70]). Multi-phase catalysts have synergetic catalytic centers to reduce the reaction energy barriers, but they suffer huge interfacial resistance due to the mismatching lattice space in heterostructures and need to pass through a long reaction route (Figure 4b[70]).[71] HER via a short-distance reaction pathway without multi-phase interface crossing is kinetically beneficial for both H_{ad} and H_2 evolution, especially in acidic conditions (Figure 4c[70]).[72] Perovskite oxides possess multiple TM sites and their high structural compatibility also enables flexible doping/defects engineering for electronic properties control.[20,73] Single-phase perovskite-oxide catalysts can form multiple atomic-level active centers on catalytic surfaces to regulate the electron-transfer behaviors of adsorption intermediates as well as balance the reaction barriers for H_{ad} and H-desorption. By atomic-scale doping, the transportation barriers of H* can be lowered, and the work function can be well tuned to reduce charge accumulation, hence improving the synergistic effects for acidic HER.[74]

Table 1. Brief summaries of the key characteristics, advantages, and limitations of different synthetic methods.

Synthetic Methods	Temperatures/ Diameters	Purity Grade	Features and Advantages	Challenges and Drawbacks	References
Conventional Solid-state Synthesis	900–1200 °C > 1000 nm	Low	Conventional simple and fast flow, and eco-friendly without poisonous gaseous emitted.	Harsh reaction conditions, large and non-uniform particle sizes, and limited specific surface area.	[65]
Hydrothermal/ Solvothermal Methods	100–240 °C (subcritical) 1000 °C (supercritical) > 100 nm	High	Relatively shorter reaction time, and easily controlled crystallinity/ morphologies.	High-temperature and high-pressure, post-annealing process is needed.	[46b,54, 66]
Electrospinning	– < 100 nm	Relatively High	Mild and low-cost, nanoscale particles, and large length-diameter ratio.	Uncontrollable porous sizes and limited specific surface area.	[57d,67]
Sol-gel Synthesis	600–1000 °C > 10 nm	Very high	Pure phase-structure, mild reaction conditions, and cost-effective.	Additional depositions/ purifications are usually needed.	[58–60,68]
PAD	25/50–500 °C 800 °C/900 °C RTA Thickness < 100 nm	High	Low cost, widely used for epitaxial composite materials and multi-layer thin films.	Relatively low coating-efficiency for a single operation.	[61,69]

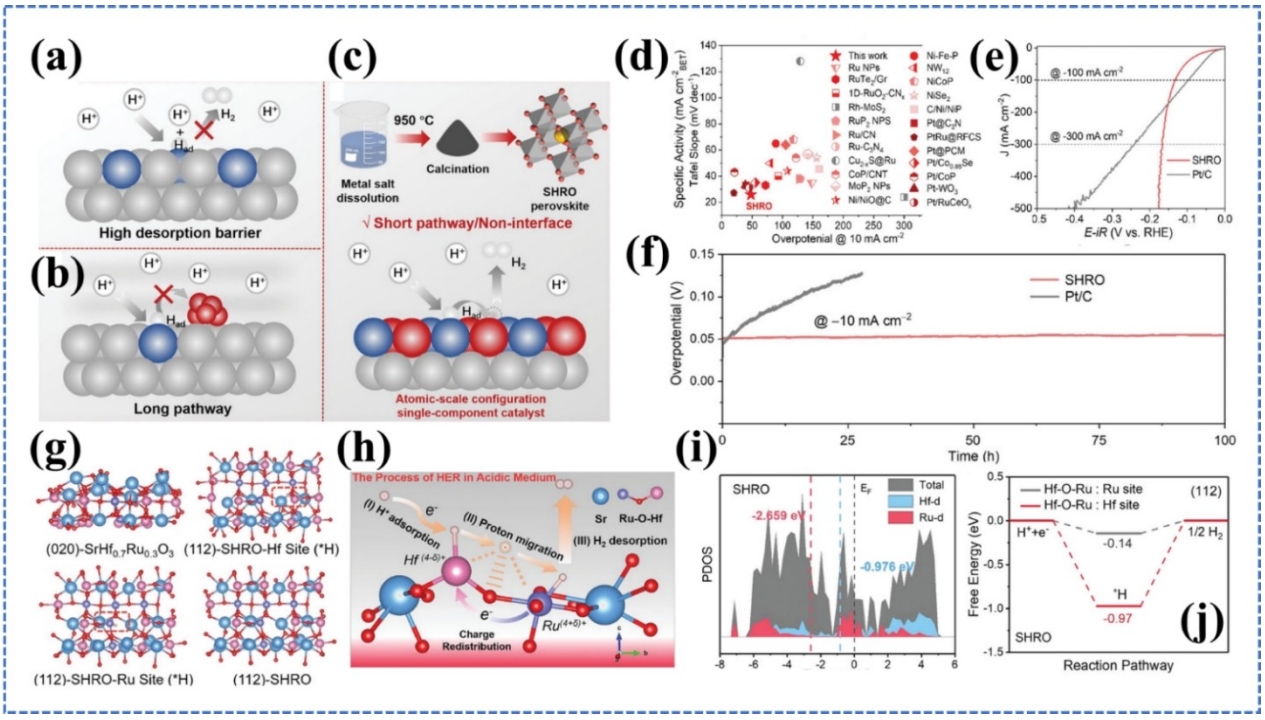

Figure 4. Schematic illustrations of (a) the HER route through in-situ H_{ad} and H_2-evolution on a single active site, (b) the long-pathway HER mechanisms involved H_{ad} and H_2-evolution on different active sites across heterojunction interface, (c) the fabrication and reaction pathway of the novel single-phase electrocatalyst in atomic-scale configuration with multiple active sites; (d) comparisons of overpotential and Tafel slope; (e) HER activity and (f) durability tests; (g) the four slabs constructed for DFT calculations; (h) schematic mechanisms of H*-migration across atomic-scale bi-metallic sites on single-phase $SrHf_{0.7}Ru_{0.3}O_{3-\delta}$ surface; (i) PDOS results; (j) reaction energy barriers for acidic HER at Ru-sites and Hf-sites of the proposed $SrHf_{0.7}Ru_{0.3}O_{3-\delta}$ catalyst.[70] Copyright 2023, Wiley-VCH.

Recently, a highly active single-component perovskite-oxide catalyst $SrHf_{0.7}Ru_{0.3}O_{3-\delta}$ has been manufactured with the atomic-scale surface configuration induced synergistic effects by sol-gel synthesis.[70] Due to the synergistic effects between Hf and Ru sites as well as the non-interface reaction route, the single-phase $SrHf_{0.7}Ru_{0.3}O_{3-\delta}$ exhibits high electrocatalytic activity with a lowered overpotential ($\eta_{10} = 48$ mV) and smaller Tafel slope (26 mV dec^{-1}) in acidic media, see Figure 4d.[70] The HER activity of $SrHf_{0.7}Ru_{0.3}O_{3-\delta}$ is −0.18 V vs reversible hydrogen electrode (RHE), superior to that of Pt/C counterpart (−0.40 V) under a high electric current density of 500 mA/cm^2, with a high durability over 100 hours (Figure 4e–f[70]). Based on DFT simulations, electrons will be donated from Ru^{4+} to Hf^{4+}, and the charge redistribution in $Ru^{(4+\delta)+}$ and $Hf^{(4-\delta)+}$ will strengthen the interactions between Hf and Ru in Hf-O–Ru structures (Figure 4g–h[70]). The Hf cations act as adsorption sites for the capture of protons and the H* will migrate to adjacent Ru cations through bridge-O atoms and then desorbed for H_2 generation. During this process, the Hf–O–Ru intermediates serve as synergistic reaction sites for electron transfer from Ru to Hf and H*-migration from Hf to Ru. The d-band center of Hf locates much closer to the Fermi level (E_F), which narrows the electron transition gap and thus contributes to the strong adsorption of H^+ at Hf sites (Figure 4i[70]). The reaction energy barrier of H-desorption at Ru sites (0.14 eV) is much lower than that at Hf sites (0.97 eV), see Figure 4j.[70] Consequently, the corporations between Hf-adsorption sites and Ru-desorption sites will lead to a minimized barrier for HER.

4.2. Perovskite Oxides for OER

The occurrence of four-electron OER involves both the O–H bond-breaking and O–O bond-forming processes, resulting in a more complex reaction mechanism than that of two-electron HER. Generally, higher overpotentials are required to be applied in OER since the energy barriers in the bond-breaking/forming reactions are relatively higher.[75] A strong correlation that accords with a volcano-like trend has been discovered between OER activity and the surface metal cations at B-sites (Figure 5a[76]). Besides, the stability of intermediate adsorbates OH* and plentiful occupied electronic states near/at the E_F also have great impacts on OER activity.[76] For AEM, since TMs act as the catalytic sites, OER is mainly decided by the binding energy between TMs and adsorbed intermediates with a thermodynamic limitation on overpotential.[77] While for LOM, since O_L atoms serve as adsorption sites, during catalytic reactions the charge-transfer process happens between the O_{2p}-orbitals of O_L atoms and O-containing intermediates, hence, making it possible to break through the theoretical limit in AEM.[44b,78]

For the deep understanding of OER mechanisms, a Sr-doped Ruddlesden-Popper (RP) phase cobaltite oxide thin-film (RP-SrX, X = 25, 50, or 75) has been manufactured to act as the model

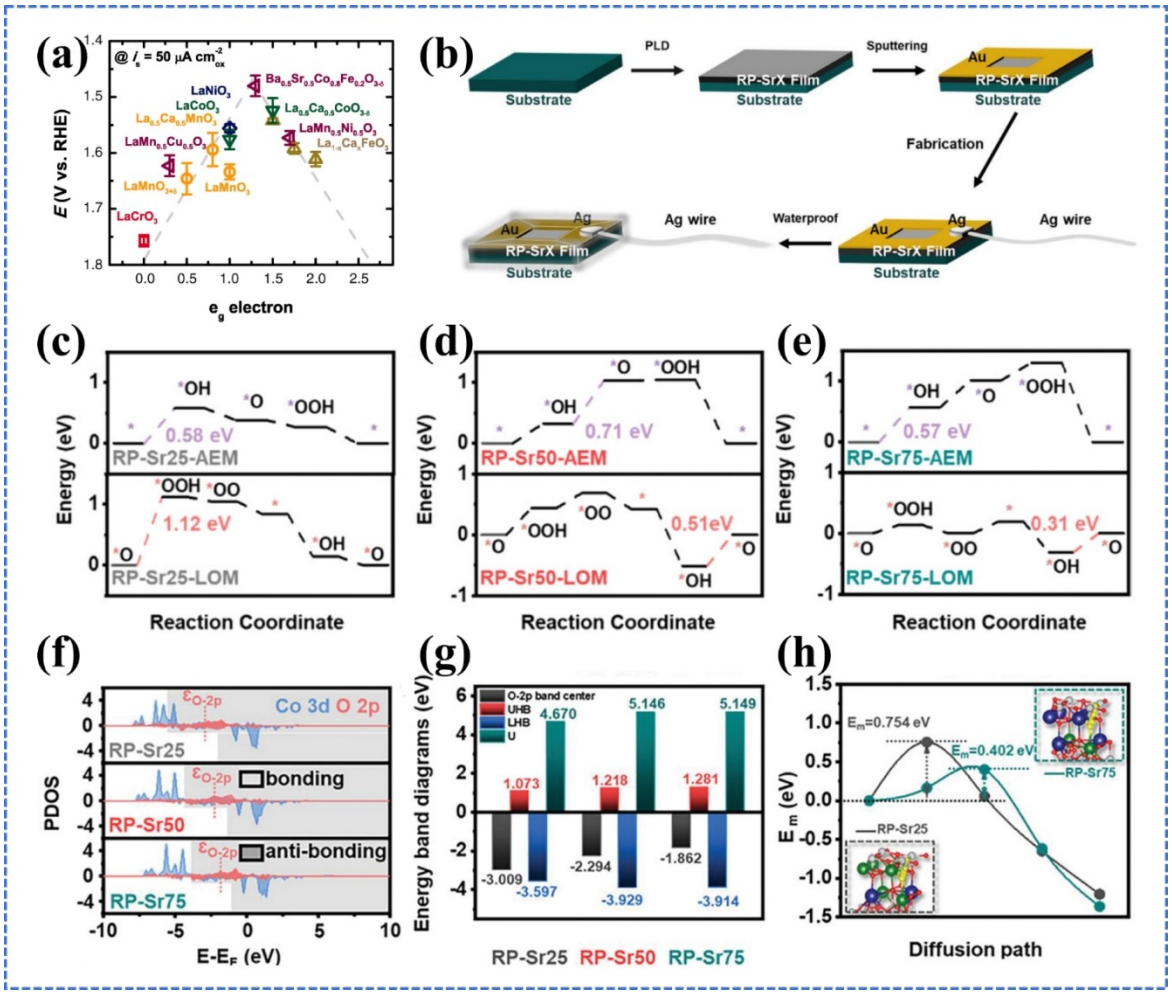

Figure 5. (a) The volcano-like relationship between OER activities and B-site cations, is described by the correlations between the overpotentials@50 μA/cm^2 and the e_g-electron occupancies of TMs.[76] Copyright 2011, American Association for the Advancement of Science. (b) Schematic fabrication of the proposed RP-SrX thin-film electrode; reaction coordinates of (c) RP–Sr25, (d) RP–Sr50, and (e) RP–Sr75 by AEM (upper) and LOM (down), respectively; (f) PDOS of O_{2p}-bands (red) and Co_{3d}-bands (blue) for the three slabs; (g) the split d-band positions of unoccupied upper Hubbard-band and electron-occupied lower Hubbard-band (UHB and LHB); (h) V_O-migration barriers E_m (eV).[79] Copyright 2023, Wiley-VCH.

electrode through pulsed-laser deposition (PLD) technique (Figure 5b[79]). It has been verified from DFT calculations that switching the reaction path from AEM to LOM will potentially decrease the reaction energy barriers for OER (Figure 5c–e[79]). With the increase of Sr-dopant concentration, the O_{2p}-orbitals of RP-SrX move up toward the E_F (Figure 5f–g[79]). The upshifting of O_{2p}-center to E_F will promote the electron-transfer process between O_L and adsorbate O atoms. With anodic voltage applied, the O_{2p}-band will further upshift to cross over E_F, causing the position alignment between the energy-level positions of O_{2p} and the standard potential of the O_2/H_2O-couple. Consequently, holes (h^+) will be produced in ligand-O atoms after the electron transfer process, which induces the oxidation of O_L atoms.[44b,78,80] Seen from Figure 5h,[79] the V_O-migration barrier of RP–Sr75 ($E_m = 0.402$ eV) is much smaller than that of RP–Sr25 ($E_m = 0.754$ eV), suggesting that the V_O-migration rates can be accelerated with the increasing of Sr-dopant concentrations.

4.3. Bifunctional Perovskite Oxides for Overall Water Splitting

There are two elementary half-reactions involved in water splitting, cathodic HER in Equation (2)/(4) and anodic OER in Equation (3)/(5), however, the slow kinetic in water dissociation particularly in complicated four-electron OER, restricts the overall reaction rate.[70,81] The catalysts will be easily corroded/dissolved in strongly acidic media, leading to reduced energy efficiency.[82] Hence, precious-metal materials such as Pt/C[83] and RuO_2/IrO_2[84] are respectively treated as candidate catalysts for electrocatalytic HER and OER in highly acidic conditions. Perovskite-oxide materials such as $SrRuO_3$ and $SrIrO_3$ are acknowledged as potential alternatives to noble-metal oxides for acidic OER because the synergistic effects of non-noble metal components will greatly increase the utilization rate of noble metals.[85] Heterostructures are also promising candidates for the establishment of multi-functional electrocatalysts since the multi-layered materials not only retain the native properties of monolayer but also induce synergistic effects between the

two joint layers.[86] Janus-metal@semiconductor constituted heterointerfaces, like Ru@V_O-enriched RuO_2,[87] and Ru@RuS_2,[88] have already been developed to act as highly active bi-functional electrocatalysts for overall water splitting. Due to the Mott-Schottky effects adjusted electronic properties in hetero-interface, a novel Ir@$SrIrO_3$ composite material has been fabricated successfully with high bi-functional electrocatalytic activities for acidic HER and OER by a top-down exsolution route (Figure 6a–b[89]).

The Ir@$SrIrO_3$–175 (annealing at 175 °C) exhibits high bi-functional activities and high operational stability, with low overpotentials of $\eta_{10}=28$ mV and $\eta_{10}=229$ mV obtained for HER and OER, respectively. According to DFT simulation results, the accumulation of electrons and charge redistributions at the Ir-$SrIrO_3$ interface (see Figure 6c[89]) will promote electron-transfer process and hence lower the reaction barriers in HER and OER. From the changes in H_{ad} Gibbs free energy (Figure 6d[89]), the Ir-$SrIrO_3$ configuration (0.34 eV) has the smallest reaction barrier for HER among the four objects studied in this work, including $SrIrO_3$, pure-Ir, $SrIrO_3$-Ir ($SrIrO_3$-layer at top), as well as Ir-$SrIrO_3$ (Ir-layer at top). Based on the calculated reaction coordinates in Figure 6e,[89] the transformation from O* to OOH* exhibits the largest energy gap for all four models, therefore it has been regarded as the RDS in four-electron OER. The $SrIrO_3$-Ir model indicates great merits in OER kinetics among the four counterparts since it possesses the lowest theoretical OER overpotential (0.72 eV), see Figure 6f.[89] Theoretically, Ir-$SrIrO_3$ possesses high HER activity while $SrIrO_3$-Ir is highly active for OER, which reveals that the novel metal/perovskite-oxide heterostructures Ir@$SrIrO_3$ are a promising bi-functional electrocatalyst for overall water splitting. It has been verified in experimental results that the Ir@$SrIrO_3$-175||Ir@$SrIrO_3$-175 exhibits a relatively lower voltage (1.49 V@10 mA/cm^2) than that of IrO_2||Pt/C benchmark (1.63 V@10 mA/cm^2), see Figure 6g.[89] From the comparisons between theoretical and experimental generation amounts of H_2/O_2, the Ir@$SrIrO_3$-175||Ir@$SrIrO_3$-175 device has an extremely high Faradaic efficiency of approximately 100%, and it also has a high durability of over 100 hours in the acidic electrolyte (see Figure 6h–i[89]). The comparisons of both the HER and OER performances of recently reported bi-functional perovskite-oxide electrocatalysts have been summarized in **Table 2**.

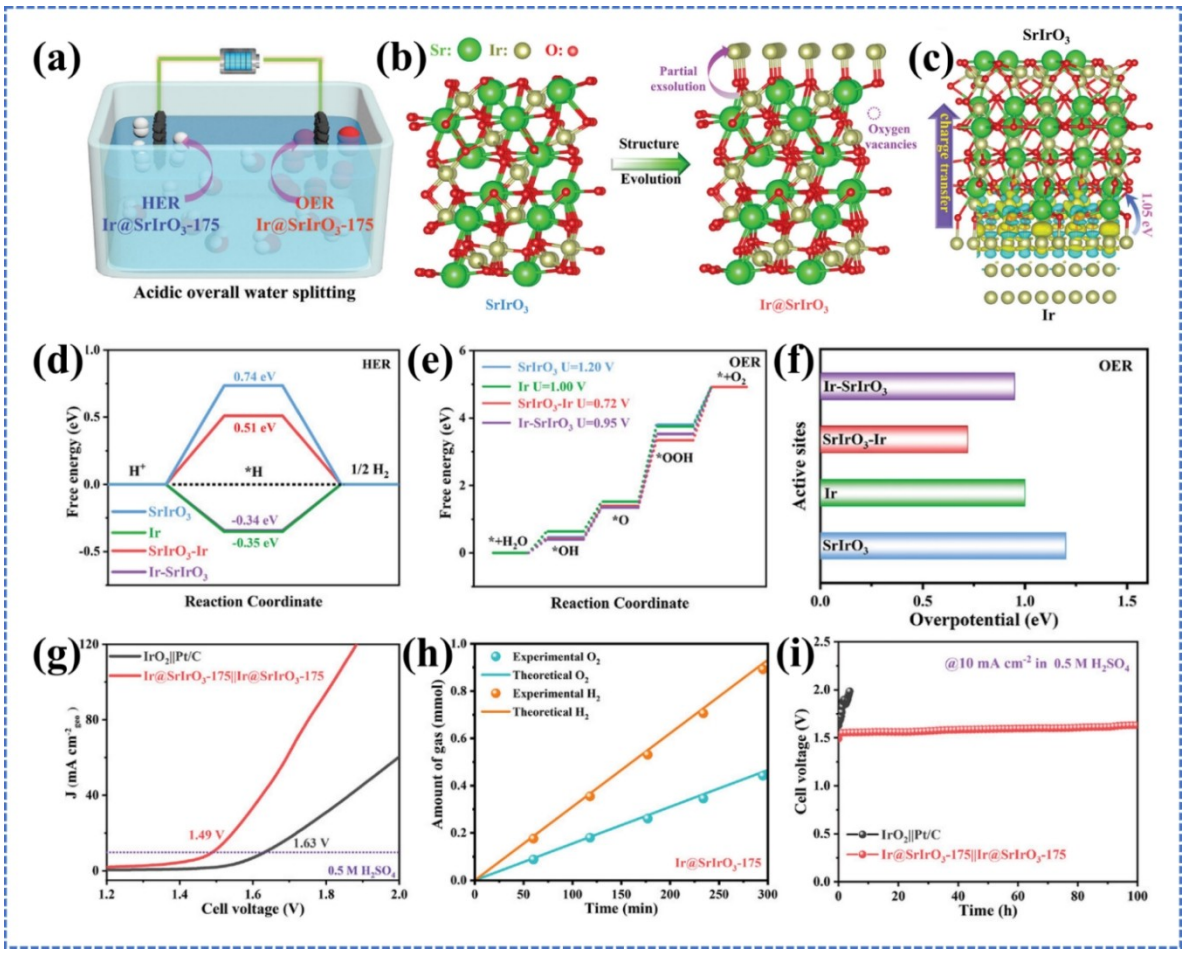

Figure 6. Schematic illustrations of (a) overall water splitting by bi-functional Ir@$SrIrO_3$–175 electrocatalysts; (b) partial exsolution process; (c) charge density difference (CDD) analysis on the interface of Ir-$SrIrO_3$ heterostructure; (d) HER barriers of $SrIrO_3$, pure-Ir, $SrIrO_3$-Ir, and Ir-$SrIrO_3$; (e) reaction coordinates for each OER step; (f) comparisons of theoretical OER overpotentials; (g) polarization plots of IrO_2||Pt/C benchmark and Ir@$SrIrO_3$-175||Ir@$SrIrO_3$-175; (h) theoretical and experimental generation amounts of H_2/O_2; (i) stability tests between the benchmark and Ir@$SrIrO_3$-175 electrodes in 0.5 H_2SO_4 via chronopotentiometry curves.[89] Copyright 2024, Wiley-VCH.

Table 2. The comparisons on both the HER and OER performances of recently reported bi-functional perovskite-oxide electrocatalysts.

Perovskite-oxide Electrocatalysts	Electrolytes	HER Overpotential (η_{10}, mV)/ Tafel Slope (mV dec^{-1})	OER Overpotential (η_{10}, mV)/ Tafel Slope (mV dec^{-1})	Ref.
Ir@$SrIrO_3$–175	0.5 M H_2SO_4	28/27.6	229/61.8	[89]
$SrCo_{0.5}Fe_{0.4}Mo_{0.1}O_{3-\delta}$	1.0 M KOH	200/72	310/46.7	[90]
$SrNb_{0.1}Co_{0.7}Fe_{0.2}O_{3-\delta}$	1.0 M KOH	262/134	390/61	[24]
$La_{0.6}Sr_{0.4}Co_{0.2}Fe_{0.8}O_{3-\delta}$	1.0 M KOH	261/-	360/56.4	[16]
$La_{0.8}Sr_{0.2}Cr_{0.69}Ni_{0.31}O_{3-\delta}$	0.1 M KOH	410/72.1	339/105	[26a]
$Pr_{0.7}Sr_{0.3}Co_{1-x}Ru_xO_3$	1.0 M KOH	319/87.32	321/118.1	[91]
$BaNiO_3$	1.0 M KOH	427/216	250/64	[92]
Sr_2IrO_4 modified $SrIrO_3$	Acidic Media	18.2/30.6	245/47.4	[93]
Ce-doped $LaCoO_3$	1.0 M KOH	305/144	380/80	[94]

5. Tuning Strategies

The reaction activities can be improved by manipulating the native lattice structures/electronic configurations of catalysts, including altering the oxidation states of site-B metals, the bonding of O_L and site-B metals, the occupation status of e_g-orbitals, and the O-p orbital/d-orbital positions with respect to the E_F.[9b,95] Especially, the e_g-orbital occupation status of surface cations will greatly affect the OER activities, and the adsorption/activation of O-containing intermediate adsorbates like O*, OH*, and OOH* can be further facilitated by rapid electron transfer.[1] Therefore, effective lattice/electronic structure controls such as doping/substitution engineering, defects engineering, morphological structure tuning, and nanotechnologies have been widely employed to increase the catalytic activity of perovskite-oxides based electrocatalysts.[1] Since HER and OER occur on electrocatalyst surfaces, the electrocatalytic performance of perovskite-oxides based electrodes also can be well tuned via surface-modification techniques, including surface reconstruction[96] and hydroxylation.[97]

5.1. Doping/Substitution Engineering

Composition engineering can be realized by external doping with different metal atoms at A-sites/B-sites, transforming the classical ABO_3 perovskite composition into a non-stoichiometry composition of $A_xA'_{1-x}$ $B_yB'_{1-y}O_{3\pm\delta}$.[11] The electronic structures of A-site cations greatly affect OER activities, and hence, A-site doping will effectively alter the OER tendency of target perovskite oxides.[98] Doping at the A-sites of perovskite oxides will cause tilt, rotation, as well as distortion in octahedral BO_6-structure, leading to variations of physicochemical properties and electronic structures.[99] In addition, the electric conductivity of catalysts will be improved by doping with low-valenced cations at A-sites.[98] Due to the inductive effect, the acid-base catalysis of material surface (the ability to donate or accept a H^+) will also be altered by selecting specific site-A dopants.[100] While the B-site TMs in perovskite oxides usually act as the catalytic active sites for HER.[48d,74,101]

5.1.1. A-Site Doping

The cation-size mismatching will cause a strong charge imbalance between external metal dopants and intrinsic A-site atoms, leading to an improved electric conductivity, optimized electronic states for B-site TMs, as well as a secondary phase created for the further improvement of catalytic activities.[102] For example, the alkaline-earth metals strontium (Sr) have been doped into the A-sites of double-perovskite $Ca_{2-x}Sr_xScRuO_6$ through solid-phase synthesis, with the formation of Ca_2ScRuO_6 ($x=0$) and $CaSrScRuO_6$ ($x=1$) respectively, see Figure 7a.[103] Under alkaline conditions, both the intrinsic Ca_2ScRuO_6 and A-site Sr doped counterpart $CaSrScRuO_6$ can serve as efficient tri-functional electrocatalysts to conduct ORR, HER and OER Figure 7b.[103] Triggered by A-site Sr-doping, the synergistic effect between the distortion of octahedral lattice and the electronic-state optimization of Ru^{5+} will contribute to the improvement of both HER and OER catalytic efficiency. Under the electric current density of 10 mA/cm^2, the overpotential required for HER by intrinsic Ca_2ScRuO_6 has been measured as 313 mV, while by $CaSrScRuO_6$, the overpotential has been reduced to 275 mV, Figure 7c.[103] Both the energy changes in H_{ad} (Volmer-step) and H_2 generation (Heyrovsky-step) processes will affect the HER barriers. According to DFT calculations, the H_{ad} reaction is the potential determining step (PDS). The doping of Sr atoms has reduced the adsorption strength between H and catalyst surface, thus resulting in a reduced overpotential Figure 7d–e.[103] Consequently, the overpotential of A-site terminated $CaSrScRuO_6$ is 0.31 V, much lower than that of non-doped Ca_2ScRuO_6 (0.43 V). As for OER, the overpotential required by A-site doped Ca_2ScRuO_6 (323 mV) is also much lower than that of the intrinsic counterpart (353 mV), see Figure 7f.[103] Compared to Ca_2ScRuO_6 (1.03 V), the overpotential of A-site terminated $CaSrScRuO_6$ (1.01 V) has been lowered by 0.02 V due to the synergistic effects of Sr-dopants and the enhanced OOH* binding in the potential determining step, see Figure 7g–h.[103]

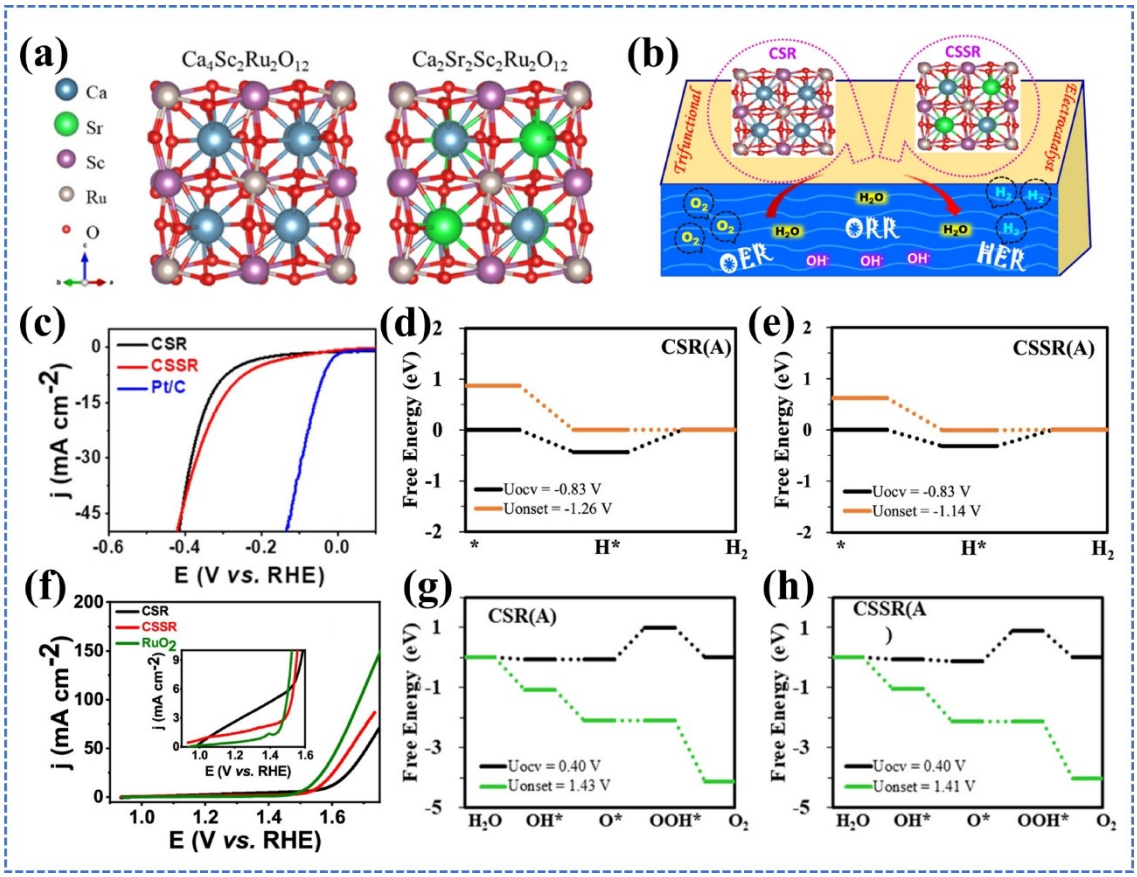

Figure 7. (a) Slabs of $Ca_4Sc_2Ru_2O_{12}$ and $Ca_2Sr_2Sc_2Ru_2O_{12}$; (b) Schematic illustrations of Ca_2ScRuO_6 (CSR) and $CaSrScRuO_6$ (CSSR) electrolyser for tri-functional electrocatalytic reactions. (c) LSVs of HER in alkaline conditions; reaction coordinates in HER for (d) CSR and (e) CSSR respectively; (f) LSVs of alkaline OER; reaction coordinates in OER for (g) CSR and (h) CSSR respectively.[103] Copyright 2022, American Chemical Society.

5.1.2. B-Site Doping

The catalytic activities can be increased remarkably with the doping of noble metals due to the synergistic effect between noble metals and non-noble TMs.[101] For instance, through conventional solid-state reaction, a single-phase $SrTi_{0.7}Ru_{0.3}O_{3-\delta}$ electrocatalyst has been synthesized by partially substituting the B-Site Ti^{3+} cations with Ru^{5+} cations in typical $SrTiO_3$ (STO) lattice. The charge redistribution induced super-exchange effects will cause 180° Ru^{5+}-O-Ti^{3+} interactions between doped $4d^3$-Ru^{5+} and intrinsic $3d^1$-Ti^{3+} cations (known as Goodenough-Karamori-Anderson's law), resulting in an improved electric conductivity. The synergistic effects among diverse active centers on the $SrTi_{0.7}Ru_{0.3}O_{3-\delta}$ surface have been studied based on DFT simulation results (Figure 8a–e[74]). The Ti-sites help reduce the kinetic energy barrier for water dissociation $H_2O^* \rightarrow OH^* + H^*$ (Figure 8b–c[74]), Ru-sites facilitate the OH*-desorption (Figure 8d[74]), and O-sites such as V_O and O_L will optimize the bi-directional energy barriers for H-adsorption (H_{ad}) and H_2 evolution (Figure 8e[74]). The alkaline HER activity of the as-prepared $SrTi_{0.7}Ru_{0.3}O_{3-\delta}$ has been remarkably improved due to the enhanced electric conductivity and synergistic catalytic sites (Figure 8f[74]), with a relatively lower overpotential (46 mV at 10 mA/cm^2) and smaller Tafel slope (40 mV/dec) obtained (Figure 8g[74]). Furthermore, the material stability has also been verified by the chronopotentiometry response of 200 hours. Another example of B-site doping enhanced alkaline OER ($\eta_{10} =$ 280 mV) is the atomic-scale Ir-doping in $LaNiO_3$ ($LaNi_{0.96}Ir_{0.04}O_3$), based on the accelerating of charge-carrier migration to catalytic surface and electron transfer to reaction intermediates via Ni–O–Ir configuration (Figure 8h–i[104]). The limited participation of O_L will restrain the structural transformation in Ir-doped $LaNiO_3$ lattice during OER, resulting in a prompted material operational durability. The addition of external B-site doping atoms will bring about modifications in the native electric structures of pristine $LaNiO_3$ and give rise to the up-shifting of d-band to E_F as well as offer additional active centers to increase the OER activity (Figure 8j–k[104]).

5.2. Defects Engineering

Defects engineering has been acknowledged as an effective way to realize accurate regulations on the electronic properties of crystalline materials at the atomic scale.[105] Induced by partial substitutions of acceptor dopants at site-A/site-B cations,[10a] V_O defects in perovskite oxides, usually represented as $ABO_{3-\delta}$, can serve as efficient catalytic active sites, especially for the

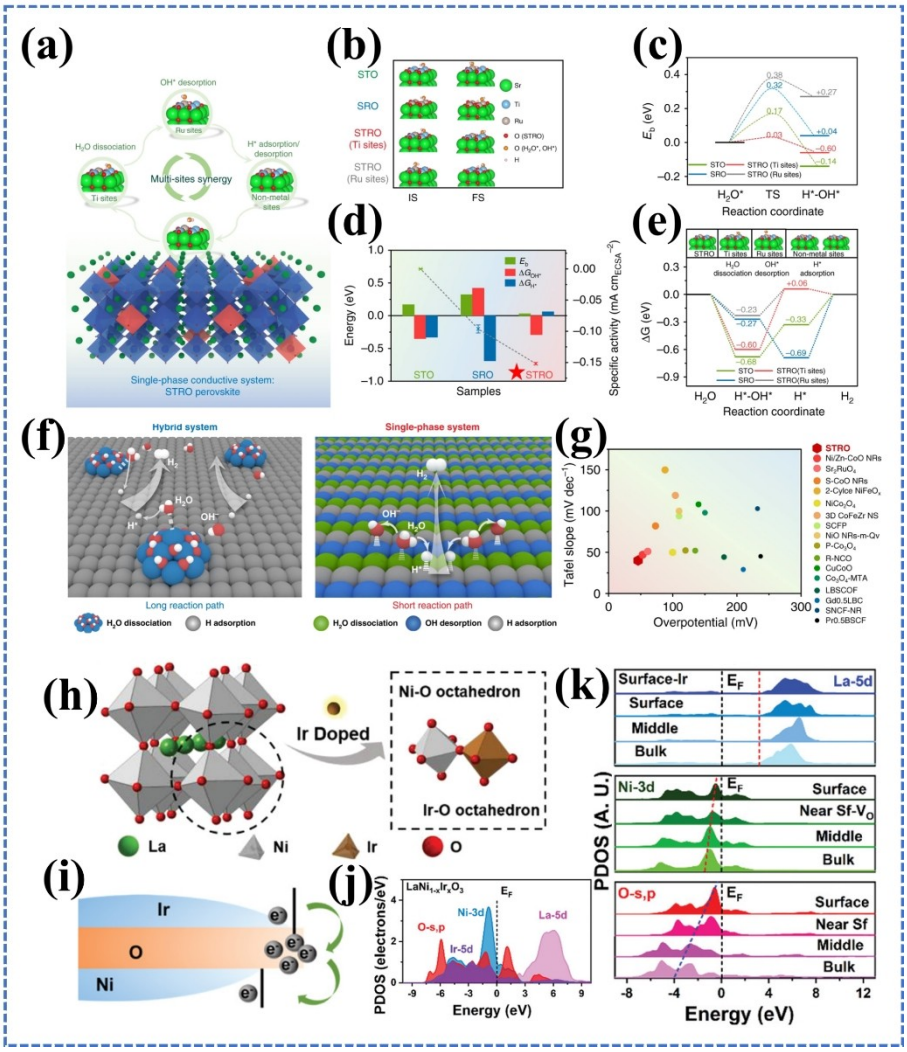

Figure 8. (a) The schematic diagram of catalytic reaction mechanisms and alkaline HER pathways at single-phase $SrTi_{0.7}Ru_{0.3}O_{3-\delta}$ surface; (b) the adsorption configurations of initial states H_2O^* and final states $H^* + OH^*$ in H_2O-dissociation stage; (c) the reaction energy barriers calculated for the breaking of H-OH bonds in the transition states of H_2O-dissociation stage (from H_2O^* to $H^* + OH^*$); (d) the correlation analysis between the calculated results (E_b, ΔG_{OH^*}, and ΔG_{H^*}) and the experimental HER-activity indicators; (e) the calculated reaction coordinates in alkaline HER; (f) the long reaction path dominated traditional hybrid system built by combining precious-metal substrates with metal-oxides (left), and the short reaction path dominated mechanism by novel single-phase system with native atomic-level synergistic catalytic sites (right); (g) comparisons on electrocatalytic HER efficiency in terms of overpotentials (η_{10}) and Tafel slopes under alkaline media.[74] Copyright 2020, Springer Nature. (h) Schematic crystalline structure of Ir-$LaNiO_3$; (i) the schematic illustration of the electron transfer process in Ni-O–Ir configuration; (j) the calculated PDOS results; (k) the site-dependent PDOS analysis from bulk to surface on La, Ni, and O atoms in Ir-doped $LaNiO_3$ lattice.[104] Copyright 2022, Wiley-VCH

adsorption and dissociation of water.[48d,106] B-site deficient perovskite oxides ($AB_{1-x}O_3$) are generally not energetically favorable without additional compensatory factors like B–B interactions.[107] The A-site deficient perovskite structures usually induce V_O defects that benefit the migration of O-ions in ABO_3 structures, and thus enhance the alkaline OER activity of electrocatalysts.[108]

For example, the substitution of Sn-dopants at A-sites in pristine-$LaNiO_3$ will induce abundant V_O defects, with $La_{0.9}Sn_{0.1}NiO_{3-\delta}$ obtained, and the doping of Sn will cause modifications in the electronic structures of O_L and greatly strengthen the covalency between O_{2p} and Ni_{3d} orbitals (Figure 9a–c[99a]). As indicated in Figure 9d–e,[99a] $La_{0.9}Sn_{0.1}NiO_{3-\delta}$ has a faster charge-extraction rate (t_{max}) and smaller attenuation constant (τ) than those of pristine-$LaNiO_3$, which verifies that the charge-transfer rate of V_O-defects rich $La_{0.9}Sn_{0.1}NiO_{3-\delta}$ is faster at the interface. Under alkaline conditions, the overpotential ($\eta_{10} = 318$ mV) of $La_{0.9}Sn_{0.1}NiO_{3-\delta}$ is much lower than that of perfect-$LaNiO_3$ ($\eta_{10} = 449$ mV), exhibiting a higher electrocatalytic activity for OER (Figure 9f[99a]). Another case of A-site deficiency induced V_O-rich perovskite oxide $Bi_{0.15}Sr_{0.85}Co_{1-x}Fe_xO_{3-\delta}$ has also explained the V_O defects accelerated charge transfer and O-ions migration mechanisms for alkaline OER.[109] There are three main OER steps that simultaneously proceed at the solid-liquid interface composed of alkaline-electrolyte and amorphous-layer (Figure 9g[109]). At the first stage, OH* will be oxidated by site-B cations/O_L with the formation of highly active intermediates (Co/Fe)–O–(OH). Subsequently, an increasing

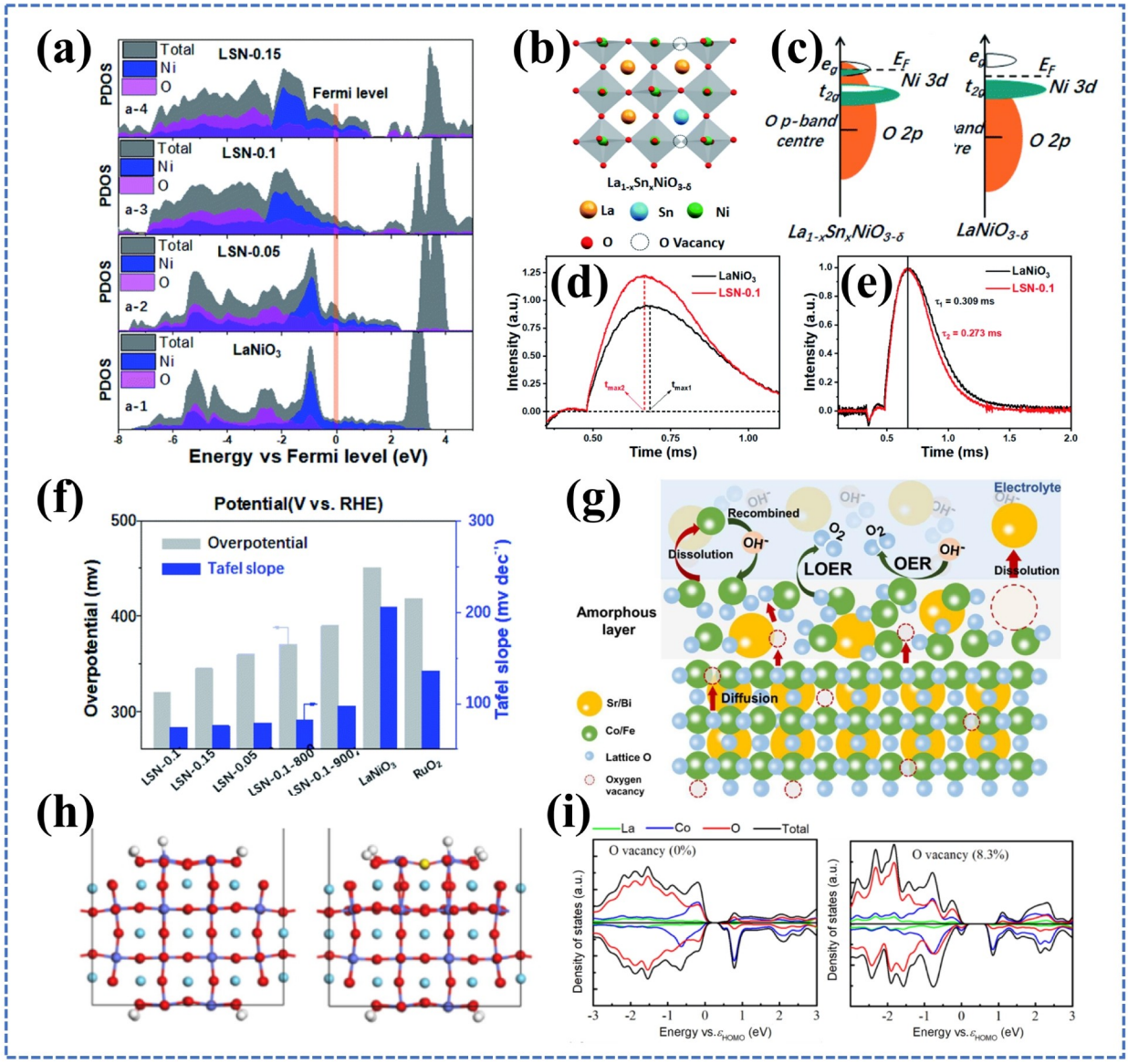

Figure 9. (a) Calculated PDOS results; (b) the lattice structure of $La_{1-x}Sn_xNiO_{3-\delta}$; (c) schematic illustrations of the overlapping between Ni_{3d} and O_{2p} orbitals for $LaNiO_3$ (left) and LSN-0.1 (right); the comparisons on (d) t_{max}, as well as (e) τ in charge recombination step; (f) the comparisons on overpotentials (η_{10}) and Tafel slopes.[99a] Copyright 2022, Royal Society of Chemistry. (g) Schematic depictions of the V_O-defects assisted OER mechanisms in $Bi_{0.15}Sr_{0.85}Co_{1-x}Fe_xO_{3-\delta}$.[109] Copyright 2023, Elsevier. (h) The lattice structures of H-adsorption on the surfaces of perfect $LaCoO_3$ (left) and $LaCoO_3$ with V_O-defects (right); (i) the calculated PDOS results of perfect $LaCoO_3$ (left) and $LaCoO_3$ with 8.3% V_O-defects (right), respectively.[112a] Copyright 2023, Elsevier.

number of site-B (Co/Fe) cations will be exposed along with the dissolution of site-A (Sr/Bi) cations, particularly Sr-cations. At the final step, the Fe-cations in the electrolyte will be re-deposited to $Bi_{0.15}Sr_{0.85}Co_{1-x}Fe_xO_{3-\delta}$ surface, contributing to the recovery of adsorption/catalytic sites for the next OER cycles. With the assistance of V_O-defects, O_L atoms can transport more quickly from bulk-phase to catalytic interface.[110] Due to the fast migration rate of O-ions in $Bi_{0.15}Sr_{0.85}Co_{0.8}Fe_{0.2}O_{3-\delta}$, the catalytic surface will be recovered quickly, hence with an enhanced OER performance and material stability obtained.[111]

Though many perovskite oxides have been reported as promising electrocatalysts for OER, the HER activities of most perovskite-oxides are relatively limited especially in alkaline solutions because of the extremely unbalanced H-adsorption and the barriers in H_2O-dissociation step.[112] The H-adsorption strength is too strong on O-sites but too weak on cation-sites. With V_O-defects generated by electrochemical activation in a novel perovskite-oxide epitaxial thin-film $LaCoO_3$, the catalytic activity for HER can be dramatically increased. The experimental characterization result suggests that the concentration of in-situ created V_O-defects on the $LaCoO_3$ surface has been raised remarkably after the electrochemical activation treatment. The correlations between the V_O-defects triggered variations in electronic structures and the increases in HER performance

have also been verified by DFT calculations, see Figure 9h–i.[112a] The increase of surface V_O-defects concentration will induce a slight up-shifting of E_F to the conduction band (CB) during electrocatalytic HER process, leading to an enhanced overall H-adsorption on $LaCoO_3$ surface. The enhanced H-adsorption on Co-sites can solve the unbalanced H-adsorption strengths on O-sites and metal-sites. In addition, V_O-defects accelerate the rate of H_2O-dissociation process which is the RDS for HER, thus facilitating the alkaline HER electrocatalytic kinetics. Under an electric current density of 0.36 mA cm^{-2}, an overpotential of 238 mV can be obtained from the electrochemical activated V_O-rich thin-film $LaCoO_3$, about 200 mV lower than that of pristine $LaCoO_3$ counterpart.

5.3. Nanostructure and Morphology Control

Prepared from conventional combustion and solid-state reactions, the particle sizes of the as-obtained perovskite-oxide crystals are relatively large owing to the high temperature applied in the crystallization process, leading to a small specific surface area that limits the catalytic efficiency. Surface morphology control has been acknowledged as another useful method to increase the electrochemical active areas of perovskite oxides. In recent decades, nanotechnologies have been broadly used to improve the surface-to-volume ratio of perovskite-oxide catalysts thus offering more surface-active sites to enhance their catalytic activities.[113] A series of nanoscale perovskite-oxide catalysts have been developed in various structural morphologies, such as nanoporous (Figure 10a[114]), nanorods (Figure 10b[56b]), and nanofibers (Figure 10c[57b]). Whereas the structures of nanomaterials are very likely to be coarsened or destroyed, particularly at a high catalytic reaction temperature. Thus, the balance between operational stability and catalytic activities should be taken into consideration during material development.[11] The optimized particle sizes and stabilized nanostructures are required to restrain electrocatalyst degradation. To increase the alkaline HER activity and material operational stability of pristine $BaCoO_{3-\delta}$, a heterostructure has been developed by assembling $Ba_3(VO_4)_2$ nanoparticles on V-doped $BaCoO_{3-\delta}$ (Figure 10d[48d]). B-site Co^{4+} cations on $BaCoO_{3-\delta}$ surface act as the catalytic centers for HER. The in-situ exsolved $Ba_3(VO_4)_2$ nanoparticles will facilitate the accumulation of Co^{4+} cations on catalyst surface, thus contributing to an improved

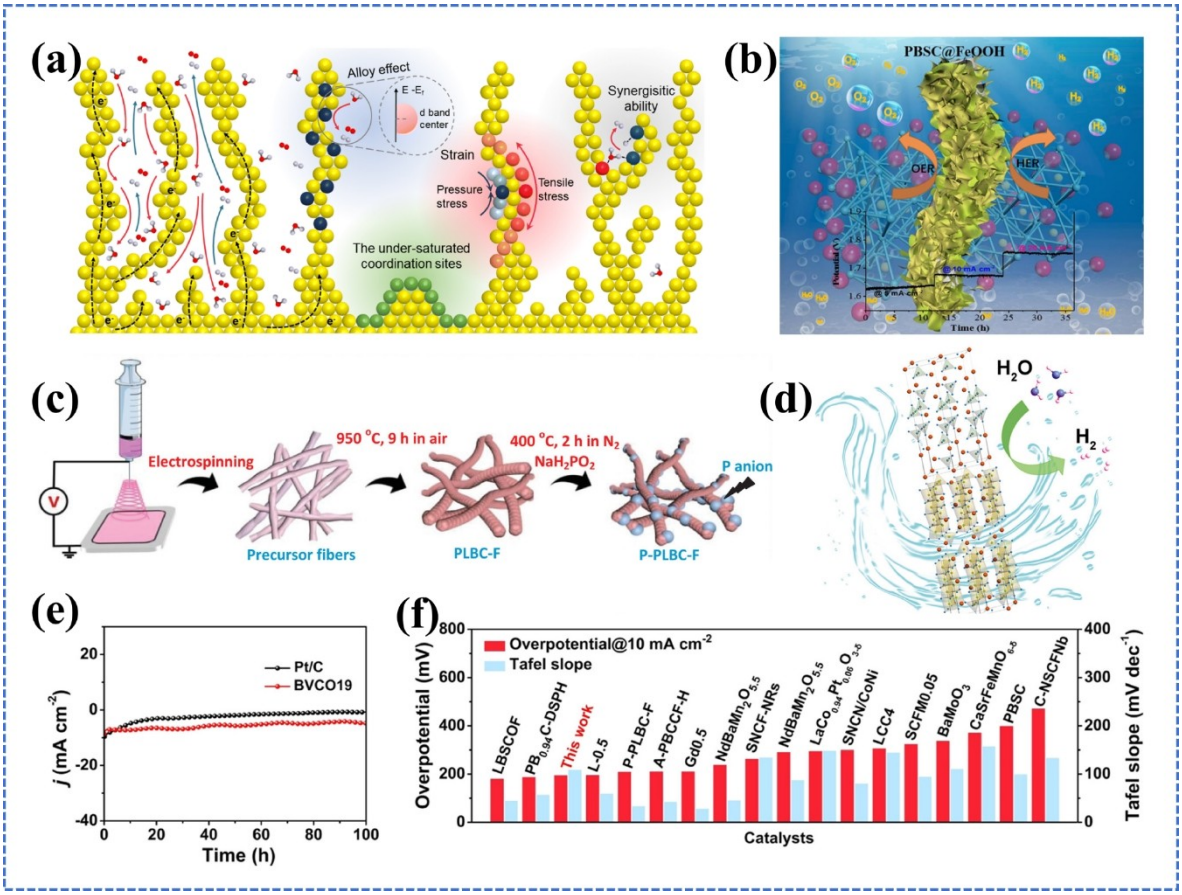

Figure 10. (a) Schematic mechanisms of de-alloyed nanoporous electrocatalysts for water splitting HER and OER, involved alloy effect, strain effect, synergistic ability, and the under-saturated coordination sites.[114] Copyright 2023, Royal Society of Chemistry. (b) Schematic illustrations of FeOOH nanoflake-decorated $PrBa_{0.5}Sr_{0.5}Co_2O_{5+\delta}$ Nanorods.[56b] Copyright 2018, American Chemical Society. (c) Phosphatizing engineering of perovskite-oxide nanofibers (P-doped $Pr_{0.5}La_{0.5}BaCo_2O_{5+\delta}$) for enhanced electrocatalytic HER.[57b] Copyright 2022, Wiley-VCH. (d) Schematic illustrations of alkaline HER mechanisms by V-$BaCoO_{3-\delta}$ decorated $Ba_3(VO_4)_2$ nanocomposite; (e) operational durability tests; (f) comparisons of overpotentials and Tafel slopes between the V-$BaCoO_{3-\delta}$ decorated $Ba_3(VO_4)_2$ nanocomposite and other highly-active perovskites.[48d] Copyright 2023, American Chemical Society.

HER activity. The formation of V_O favors the first two HER stages, water adsorption and subsequent dissociation. Through the valency control on Co and V cations, the number of V_O can be increased to realize the charge balance. The synergistic effect between Co^{4+} cations and V_O defects has greatly improved the alkaline HER activity of V-doped $BaCoO_{3-\delta}$, with lower overpotential ($\eta_{10} = 194$ mV) and higher stability (at least 100 hours under chronoamperometric testing), obtained, surpassing most of the non-noble perovskite-oxide counterparts (Figure 10e–f[48d]).

6. Summary and Outlook

This review covers the basic mechanisms involved in HER and OER, the effects of various synthetic methods on perovskite-oxide morphologies, recently reported perovskite-oxide electrocatalysts, and frequently-used tuning strategies on enhancing the electrocatalytic HER/OER activities of existing perovskite-oxides. In terms of material utilization rate and energy efficiency, mild synthetic methods such as electrospinning and sol-gel synthesis are superior to typical approaches under harsh conditions for nano-scale morphology controls. The degradation of perovskite-oxide electrocatalysts in highly acidic media still hinders their applications in water splitting. The noble-metal based electrocatalysts, such as HER benchmark Pt/C and typical OER catalysts RuO_2/IrO_2, exhibit strong resistant capacity to acid corrosion but the high-cost of noble metal components has limited their industrialized applications. Multi-metal perovskite oxides are promising alternatives to noble-metal oxides for acidic HER/OER since the synergic effects of assistant non-noble metals will remarkably enhance the energy efficiency of noble metal components and thus lower the material costs. The multi-metal active sites on single-phase perovskite oxides surface enable a kinetic favorable short reaction route for H* migration and electron transfer. The cooperation between multi-metal sites in perovskite oxides can potentially minimize reaction energy barriers, especially in HER, and thus reduce the overpotential required for the conducting of electrocatalytic water splitting reactions. Furthermore, due to the interfacial charge redistributions induced electronic structure modulation, the construction of metal/perovskite-oxide heterojunctions is another useful strategy for improving electrocatalytic performance. As for existing perovskite-oxide electrocatalysts, heteroatomic doping, defects engineering, and morphology control have been acknowledged as effective methods for electronic property regulations. In particular, the doping of cations usually triggers the creation of V_O-defects that can cooperate with O_L atoms to facilitate the LOM dominated OER.

Experimental HER and OER are usually conducted upon rotating-disk electrodes with a very fast rotation rate, as a result, the evaluated area is very limited. Besides, the reaction conditions set for the laboratory durability testing cannot satisfy the criteria in large-scale industrial production. In industrial applications, higher electric current density (0.5 A/cm^2–2.0 A/cm^2) as well as higher temperature ambience (80 °C) are usually required. Though perovskite-oxide materials can be manufactured in different forms and sizes by specific synthetic methods, the mass production of perovskite-oxide electrocatalysts with controllable and uniform diameters is relatively hard to achieve at this moment.[115] Especially for the large-scale preparations of perovskite-oxide core-shell nanoparticles with high specific surface areas and highly porous structures. In laboratory studies, to achieve a high mass-activity ratio, the loading amount of perovskite-oxides on carbon substrates is usually very small. However, to realize high electrolytic efficiency and satisfactory material stability, the high loading and uniform distribution of electrocatalysts on electrodes are also necessary in practical applications. Thus, besides the combination with membrane electrodes, investigations under industrialization conditions are required to be implemented together with DFT calculations based on machine learning predictions for the directionally developing of promising perovskite-oxide nanofiber electrocatalysts that satisfy large-scale industrial applications.[2,116]

Many perovskite-oxides exhibit limited stability in acidic media.[115] Thus, finding stable perovskite-oxide electrocatalysts within a broad pH range is an important issue from the perspectives of costs and efficiency. The electric conduction channels can be magnified by carbon-based supports. Hence, the electrochemical activity can be enhanced due to the construction of perovskite-oxide/carbon composite materials. Whereas with relatively high applied potential, electrochemical oxidation is very likely to occur especially in OER, causing the decrease of catalytic centers. Restraining the electrochemical oxidation in the electrocatalytic processes and exploring novel corrosion-resistant substrates are very significant. Generally, the laboratory stability evaluation of candidate perovskite-oxide electrocatalysts last for 100 hours. However, for industrial productions, the electrocatalysts will function under an electric current density much higher than that in laboratory testing for hundreds of hours. Thus, developing a wide pH range applicable and durable perovskite-oxide electrocatalysts to satisfy the long-term stability criteria of industries is very likely to be the recent research hotspot.

To sum up, the electrocatalytic HER/OER mechanisms and regulating strategies that this work focused on will offer a comprehensive reference for both theoretical and experimental researchers to develop novel perovskite-oxide electrocatalysts for efficient water splitting.

Acknowledgements

The authors gratefully acknowledge the support from the National Key R&D Program of China (2021YFA1501101), Research Grant Council of Hong Kong (15304023, 15304724, C1003–23Y), National Natural Science Foundation of China/Research Grant Council of Hong Kong Joint Research Scheme (N_PolyU502/21), National Natural Science Foundation of China/Research Grants Council of Hong Kong Collaborative Research Scheme (CRS_PolyU504/22), the funding for Projects of Strategic Importance of The Hong Kong Polytechnic University (Project Code: 1-ZE2 V), Shenzhen Fundamental Research Scheme-General Program (JCYJ20220531090807017), and Natu-

ral Science Foundation of Guangdong Province (2023 A1515012219).

Conflict of Interests

The authors declare no conflict of interest.

Data Availability Statement

The data that support the findings of this study are available from the corresponding author upon reasonable request.

Keywords: Perovskite oxides · Electrocatalysis · HER · OER · Mechanisms

[1] D. Liu, P. Zhou, H. Bai, H. Ai, X. Du, M. Chen, D. Liu, W. F. Ip, K. H. Lo, C. T. Kwok, S. Chen, S. Wang, G. Xing, X. Wang, H. Pan, *Small* **2021**, *17*, 2101605.
[2] Y. Wang, Y. Jiang, Y. Zhao, X. Ge, Q. Lu, T. Zhang, D. Xie, M. Li, Y. Bu, *Chem. Eng. J.* **2023**, *451*, 138710.
[3] H. Xu, H. Shang, C. Wang, Y. Du, *Coord. Chem. Rev.* **2020**, *418*, 213374.
[4] a) X. Wang, X. Zhang, G. Fu, Y. Tang, *Mater. Today Energy* **2021**, *22*, 100850; b) Q. Shao, P. Wang, T. Zhu, X. Huang, *Acc. Chem. Res.* **2019**, *52*, 3384–3396.
[5] A. H. Al-Naggar, N. M. Shinde, J.-S. Kim, R. S. Mane, *Coord. Chem. Rev.* **2023**, *474*, 214864.
[6] Y. Liu, S. Jiang, S. Li, L. Zhou, Z. Li, J. Li, M. Shao, *Appl. Catal., B* **2019**, *247*, 107–114.
[7] F. Du, L. Shi, Y. Zhang, T. Li, J. Wang, G. Wen, A. Alsaedi, T. Hayat, Y. Zhou, Z. Zou, *Appl. Catal., B* **2019**, *253*, 246–252.
[8] Q. Xu, H. Jiang, H. Zhang, Y. Hu, C. Li, *Appl. Catal., B* **2019**, *242*, 60–66.
[9] a) Y. Guo, X. Yu, Q. Yu, Y. Li, Y. Liu, C. Zhao, L. Jin, Z. Liu, J. Li, *J. Phys. Chem. C* **2022**, *126*, 8065–8078; b) L. Lu, M. Sun, T. Wu, Q. Lu, B. Chen, C. H. Chan, H. H. Wong, B. Huang, *Inorg. Chem. Front.* **2024**, *11*, 6853–6861; c) L. Lu, M. Sun, T. Wu, Q. Lu, B. Chen, C. H. Chan, H. H. Wong, B. Huang, *Front. Chem.* **2023**, *11*, 1197010; d) M. Umer, S. Umer, M. Zafari, M. Ha, R. Anand, A. Hajibabaei, A. Abbas, G. Lee, K. S. Kim, *J. Mater. Chem. A* **2022**, *10*, 6679–6689; e) M. Xu, X. Zhang, Y. Liu, X. Zhao, Y. Liu, R. Wu, J. Wang, *ChemPhysChem* **2020**, *21*, 2651–2659; f) L. Lu, M. Sun, T. Wu, Q. Lu, B. Chen, C. H. Chan, H. H. Wong, B. Huang, *Small Methods* **2023**, *7*, 2300430.
[10] a) H. Arandiyan, S. S. Mofarah, C. C. Sorrell, E. Doustkhah, B. Sajjadi, D. Hao, Y. Wang, H. Sun, B.-J. Ni, M. Rezaei, Z. Shao, T. Maschmeyer, *Chem. Soc. Rev.* **2021**, *50*, 10116–10211; b) B. Hua, M. Li, J.-L. Luo, *Nano Energy* **2018**, *49*, 117–125.
[11] C. Si, W. Zhang, Q. Lu, E. Guo, Z. Yang, J. Chen, X. He, J. Luo, *Catalysts* **2022**, *12*(6), 601.
[12] L. Lu, M. Sun, T. Wu, Q. Lu, B. Huang, *Chem. Commun.* **2021**, *57*, 9366–9369.
[13] J. T. Mefford, W. G. Hardin, S. Dai, K. P. Johnston, K. J. Stevenson, *Nat. Mater.* **2014**, *13*, 726–732.
[14] J. H. Kim, S. Yoo, R. Murphy, Y. Chen, Y. Ding, K. Pei, B. Zhao, G. Kim, Y. Choi, M. Liu, *Energy Environ. Sci.* **2021**, *14*, 1506–1516.
[15] a) Y. Liu, H. Huang, L. Xue, J. Sun, X. Wang, P. Xiong, J. Zhu, *Nanoscale* **2021**, *13*, 19840–19856; b) Y. Liu, C. Ye, S.-N. Zhao, Y. Wu, C. Liu, J. Huang, L. Xue, J. Sun, W. Zhang, X. Wang, P. Xiong, J. Zhu, *Nano Energy* **2022**, *99*, 107344.
[16] R. Zong, Y. Fang, C. Zhu, X. Zhang, L. Wu, X. Hou, Y. Tao, J. Shao, *ACS Appl. Mater. Interfaces* **2021**, *13*, 42852–42860.
[17] B. Hua, M. Li, Y.-F. Sun, Y.-Q. Zhang, N. Yan, J. Chen, T. Thundat, J. Li, J.-L. Luo, *Nano Energy* **2017**, *32*, 247–254.
[18] Q. A. Islam, R. Majee, S. Bhattacharyya, *J. Mater. Chem. A* **2019**, *7*, 19453–19464.
[19] a) Y. Duan, S. Sun, S. Xi, X. Ren, Y. Zhou, G. Zhang, H. Yang, Y. Du, Z. J. Xu, *Chem. Mater.* **2017**, *29*, 10534–10541; b) R. Majee, S. Chakraborty, H. G. Salunke, S. Bhattacharyya, *ACS Appl. Energy Mater.* **2018**, *1*, 3342–3350.
[20] X. Xu, Y. Chen, W. Zhou, Z. Zhu, C. Su, M. Liu, Z. Shao, *Adv. Mater.* **2016**, *28*, 6442–6448.
[21] J.-I. Jung, S. Park, M.-G. Kim, J. Cho, *Adv. Energy Mater.* **2015**, *5*, 1501560.
[22] R. Khan, M. T. Mehran, S. R. Naqvi, A. H. Khoja, K. Mahmood, F. Shahzad, S. Hussain, *Int. J. Energy Res.* **2020**, *44*, 9714–9747.
[23] D. Chen, C. Chen, Z. M. Baiyee, Z. Shao, F. Ciucci, *Chem. Rev.* **2015**, *115*, 9869–9921.
[24] Y. Zhu, W. Zhou, Y. Zhong, Y. Bu, X. Chen, Q. Zhong, M. Liu, Z. Shao, *Adv. Energy Mater.* **2017**, *7*, 1602122.
[25] a) M. Prabu, K. Ketpang, S. Shanmugam, *Nanoscale* **2014**, *6*, 3173–3181; b) A. Greiner, J. H. Wendorff, *Angew. Chem. Int. Ed.* **2007**, *46*, 5670–5703.
[26] a) Y. Wang, Z. Wang, C. Jin, C. Li, X. Li, Y. Li, R. Yang, M. Liu, *Electrochim. Acta* **2019**, *318*, 120–129; b) T. Zhu, H. E. Troiani, L. V. Mogni, M. Han, S. A. Barnett, *Joule* **2018**, *2*, 478–496.
[27] Y. Jiao, Y. Zheng, M. Jaroniec, S. Z. Qiao, *Chem. Soc. Rev.* **2015**, *44*, 2060–2086.
[28] J. Wei, M. Zhou, A. Long, Y. Xue, H. Liao, C. Wei, Z. J. Xu, *Nano-Micro Lett.* **2018**, *10*, 75.
[29] L. Li, P. Wang, Q. Shao, X. Huang, *Chem. Soc. Rev.* **2020**, *49*, 3072–3106.
[30] L.-f. Shen, B.-a. Lu, Y.-y. Li, J. Liu, Z.-c. Huang-fu, H. Peng, J.-y. Ye, X.-m. Qu, J.-m. Zhang, G. Li, W.-b. Cai, Y.-x. Jiang, S.-g. Sun, *Angew. Chem. Int. Ed.* **2020**, *59*, 22397–22402.
[31] a) Q. Liang, G. Brocks, A. Bieberle-Hütter, *J. Phys.: Energy* **2021**, *3*, 026001; b) X. Zhang, A. Bieberle-Hütter, *ChemSusChem* **2016**, *9*, 1223–1242; c) E. Fabbri, A. Habereder, K. Waltar, R. Kötz, T. J. Schmidt, *Catal. Sci. Technol.* **2014**, *4*, 3800–3821.
[32] a) J. K. Nørskov, J. Rossmeisl, A. Logadottir, L. Lindqvist, J. R. Kitchin, T. Bligaard, H. Jónsson, *J. Phys. Chem. B* **2004**, *108*, 17886–17892; b) J. Rossmeisl, Z. W. Qu, H. Zhu, G. J. Kroes, J. K. Nørskov, *J. Electroanal. Chem.* **2007**, *607*, 83–89.
[33] a) N. Snir, N. Yatom, M. Caspary Toroker, *Comput. Mater. Sci.* **2019**, *160*, 411–419; b) Y. Zuo, Y. Liu, J. Li, R. Du, X. Han, T. Zhang, J. Arbiol, N. J. Divins, J. Llorca, N. Guijarro, K. Sivula, A. Cabot, *Chem. Mater.* **2019**, *31*, 7732–7743.
[34] a) I. Yamada, A. Takamatsu, K. Asai, T. Shirakawa, H. Ohzuku, A. Seno, T. Uchimura, H. Fujii, S. Kawaguchi, K. Wada, H. Ikeno, S. Yagi, *J. Phys. Chem. C* **2018**, *122*, 27885–27892; b) Q. Ma, S. Mu, *Interdiscip. Mater.* **2023**, *2*, 53–90; c) V. Tripkovic, H. A. Hansen, J. M. Garcia-Lastra, T. Vegge, *J. Phys. Chem. C* **2018**, *122*, 1135–1147.
[35] N.-T. Suen, S.-F. Hung, Q. Quan, N. Zhang, Y.-J. Xu, H. M. Chen, *Chem. Soc. Rev.* **2017**, *46*, 337–365.
[36] a) T. Wu, S. Sun, J. Song, S. Xi, Y. Du, B. Chen, W. A. Sasangka, H. Liao, C. L. Gan, G. G. Scherer, L. Zeng, H. Wang, H. Li, A. Grimaud, Z. J. Xu, *Nature Catal.* **2019**, *2*, 763–772; b) X. Liu, J. Meng, J. Zhu, M. Huang, B. Wen, R. Guo, L. Mai, *Adv. Mater.* **2021**, *33*, 2007344.
[37] M. Wohlfahrt-Mehrens, J. Heitbaum, *J. Electroanal. Chem. Interfacial Electrochem.* **1987**, *237*, 251–260.
[38] O. Diaz-Morales, F. Calle-Vallejo, C. de Munck, M. T. M. Koper, *Chem. Sci.* **2013**, *4*, 2334–2343.
[39] J. S. Yoo, X. Rong, Y. Liu, A. M. Kolpak, *ACS Catal.* **2018**, *8*, 4628–4636.
[40] a) Z.-F. Huang, S. Xi, J. Song, S. Dou, X. Li, Y. Du, C. Diao, Z. J. Xu, X. Wang, *Nature Commun.* **2021**, *12*, 3992; b) Z.-F. Huang, J. Song, Y. Du, S. Xi, S. Dou, J. M. V. Nsanzimana, C. Wang, Z. J. Xu, X. Wang, *Nat. Energy* **2019**, *4*, 329–338.
[41] a) Y. Wen, P. Chen, L. Wang, S. Li, Z. Wang, J. Abed, X. Mao, Y. Min, C. T. Dinh, P. D. Luna, R. Huang, L. Zhang, L. Wang, L. Wang, R. J. Nielsen, H. Li, T. Zhuang, C. Ke, O. Voznyy, Y. Hu, Y. Li, W. A. Goddard Iii, B. Zhang, H. Peng, E. H. Sargent, *J. Am. Chem. Soc.* **2021**, *143*, 6482–6490; b) A. Zagalskaya, V. Alexandrov, *ACS Catal.* **2020**, *10*, 3650–3657; c) Y. Yao, S. Hu, W. Chen, Z.-Q. Huang, W. Wei, T. Yao, R. Liu, K. Zang, X. Wang, G. Wu, W. Yuan, T. Yuan, B. Zhu, W. Liu, Z. Li, D. He, Z. Xue, Y. Wang, X. Zheng, J. Dong, C.-R. Chang, Y. Chen, X. Hong, J. Luo, S. Wei, W.-X. Li, P. Strasser, Y. Wu, Y. Li, *Nat. Catal.* **2019**, *2*, 304–313.
[42] Q. Wu, K. Jiang, J. Han, D. Chen, M. Luo, J. Lan, M. Peng, Y. Tan, *Sci. China Mater.* **2022**, *65*, 1262–1268.
[43] V. Kumar, R. Kumar, D. K. Shukla, S. Gautam, K. Hwa Chae, R. Kumar, *J. Appl. Phys.* **2013**, *114*, 073704.
[44] a) S. Nakayama, *J. Mater. Sci.* **2001**, *36*, 5643–5648; b) J. T. Mefford, X. Rong, A. M. Abakumov, W. G. Hardin, S. Dai, A. M. Kolpak, K. P. Johnston, K. J. Stevenson, *Nat. Commun.* **2016**, *7*, 11053.
[45] C. Zhu, A. Nobuta, I. Nakatsugawa, T. Akiyama, *Int. J. Hydrog. Energy* **2013**, *38*, 13238–13248.

[46] a) S. Bie, Y. Zhu, J. Su, C. Jin, S. Liu, R. Yang, J. Wu, *J. Mater. Chem. A* **2015**, *3*, 22448–22453; b) T. D. Thanh, N. D. Chuong, J. Balamurugan, H. Van Hien, N. H. Kim, J. H. Lee, *Small* **2017**, *13*, 1701884.
[47] Y. Zheng, X. Feng, D. Lin, E. Wu, Y. Luo, Y. You, B. Huang, Q. Qian, Q. Chen, *Chin. J. Chem.* **2020**, *38*, 144–150.
[48] a) S. Zhou, X. Miao, X. Zhao, C. Ma, Y. Qiu, Z. Hu, J. Zhao, L. Shi, J. Zeng, *Nat. Commun.* **2016**, *7*, 11510; b) C.-F. Chen, G. King, R. M. Dickerson, P. A. Papin, S. Gupta, W. R. Kellogg, G. Wu, *Nano Energy* **2015**, *13*, 423–432; c) S. Zhuang, C. Huang, K. Huang, X. Hu, F. Tu, H. Huang, *Electrochem. Commun.* **2011**, *13*, 321–324; d) D. Zhou, F. Le, W. Jia, X. Chen, *Inorg. Chem.* **2023**, *62*, 8001–8009; e) Z. Zhang, W. Zhou, Z. Yang, J. Jiang, D. Chen, Z. Shao, *Int. J. Hydrogen Energy* **2020**, *45*, 24859–24869.
[49] G. F. Zou, J. Zhao, H. M. Luo, T. M. McCleskey, A. K. Burrell, Q. X. Jia, *Chem. Soc. Rev.* **2013**, *42*, 439–449.
[50] H. Wang, M. Zhou, P. Choudhury, H. Luo, *Appl. Mater. Today* **2019**, *16*, 56–71.
[51] C. Si, C. Zhang, J. Sunarso, Z. Zhang, *J. Mater. Chem. A* **2018**, *6*, 19979–19988.
[52] S. Ivanova, A. Senyshyn, E. Zhecheva, K. Tenchev, R. Stoyanova, H. Fuess, *J. Solid State Chem.* **2010**, *183*, 940–950.
[53] A. G. Prince, L. Durai, S. Badhulika, *New J. Chem.* **2023**, *47*, 3870–3879.
[54] H.-L. Ge, Z.-Y. Wang, G.-R. Li, S. Liu, X.-P. Gao, *Electrochim. Acta* **2022**, *424*, 140670.
[55] a) G. Liu, H. Chen, L. Xia, S. Wang, L.-X. Ding, D. Li, K. Xiao, S. Dai, H. Wang, *ACS Appl. Mater. Interfaces* **2015**, *7*, 22478–22486; b) P. Li, J. Zhang, Q. Yu, J. Qiao, Z. Wang, D. Rooney, W. Sun, K. Sun, *Electrochim. Acta* **2015**, *165*, 78–84.
[56] a) B. Hua, M. Li, Y.-Q. Zhang, Y.-F. Sun, J.-L. Luo, *Adv. Energy Mater.* **2017**, *7*, 1700666; b) Z. Zhang, B. He, L. Chen, H. Wang, R. Wang, L. Zhao, Y. Gong, *ACS Appl. Mater. Interfaces* **2018**, *10*, 38032–38041.
[57] a) J. Bian, R. Su, Y. Yao, J. Wang, J. Zhou, F. Li, Z. L. Wang, C. Sun, *ACS Appl. Energy Mater.* **2019**, *2*, 923–931; b) S. Li, T. Xia, Y. Dou, Y. Xie, J. Wang, H. Zhao, L. Huo, *Adv. Funct. Mater.* **2022**, *32*, 2112164; c) Z. Li, J.-G. Li, X. Ao, H. Sun, H. Wang, M.-F. Yuen, C. Wang, *Electrochim. Acta* **2020**, *334*, 135638; d) Z. Li, K.-H. Xue, J. Wang, J.-G. Li, X. Ao, H. Sun, X. Song, W. Lei, Y. Cao, C. Wang, *ACS Appl. Mater. Interfaces* **2020**, *12*, 41259–41268.
[58] D. Bokov, A. Turki Jalil, S. Chupradit, W. Suksatan, M. Javed Ansari, I. H. Shewael, G. H. Valiev, E. Kianfar, *Adv. Mater. Sci. Eng.* **2021**, *2021*, 5102014.
[59] A. De, M. S. Kim, A. Adhikari, R. Patel, S. Kundu, *J. Mater. Chem. A* **2024**, *12*, 19720–19756.
[60] X. Xu, W. Wang, W. Zhou, Z. Shao, *Small Methods* **2018**, *2*, 1800071.
[61] J. M. Vila-Fungueiriño, B. Rivas-Murias, J. Rubio-Zuazo, A. Carretero-Genevrier, M. Lazzari, F. Rivadulla, *J. Mater. Chem. C* **2018**, *6*, 3834–3844.
[62] A. K. Burrell, T. Mark McCleskey, Q. X. Jia, *Chem. Commun.* **2008**, *11*, 1271–1277.
[63] Q. X. Jia, T. M. McCleskey, A. K. Burrell, Y. Lin, G. E. Collis, H. Wang, A. D. Q. Li, S. R. Foltyn, *Nat. Mater.* **2004**, *3*, 529–532.
[64] H. Wang, C. Frontera, B. Martínez, N. Mestres, *Materials* **2020**, *13*, 4966.
[65] a) D. D. Athayde, D. F. Souza, A. M. A. Silva, D. Vasconcelos, E. H. M. Nunes, J. C. Diniz da Costa, W. L. Vasconcelos, *Ceram. Int.* **2016**, *42*, 6555–6571; b) H. Wang, M. Zhou, P. Choudhury, H. Luo, *Appl. Mater. Today* **2019**, *16*, 56–71; c) H. Li, J. Yu, Y. Gong, N. Lin, Q. Yang, X. Zhang, Y. Wang, *Separ. Purif. Technol.* **2023**, *307*, 122716; d) V. Kumar, R. Kumar, D. K. Shukla, S. Gautam, K. Hwa Chae, R. Kumar, *J. Appl. Phys.* **2013**, *114*, 073704.
[66] a) M. Shandilya, R. Rai, J. Singh, *Adv. Appl. Ceram.* **2016**, *115*, 354–376; b) S. H. Feng, G. H. Li, *Modern Inorganic Synthetic Chemistry (Second Edition)* (Eds: R. Xu, Y. Xu), Elsevier, Amsterdam **2017**, 73–104.
[67] X. Huang, G. Zhao, G. Wang, J. T. S. Irvine, *Chem. Sci.* **2018**, *9*, 3623–3637.
[68] X. Wang, M. Ahmad, H. Sun, *Materials (Basel)* **2017**, *10*, 1304.
[69] a) Y. Lin, J. Xie, H. Wang, Y. Li, C. Chavez, S. Lee, S. R. Foltyn, S. A. Crooker, A. K. Burrell, T. M. McCleskey, Q. X. Jia, *Thin Solid Films* **2005**, *492*, 101–104; b) J. M. Vila-Fungueiriño, A. Gómez, J. Antoja-Lleonart, J. Gázquez, C. Magén, B. Noheda, A. Carretero-Genevrier, *Nanoscale* **2018**, *10*, 20155–20161; c) M. A. Garcia, M. N. Ali, T. Parsons-Moss, P. D. Ashby, H. Nitsche, *Thin Solid Films* **2008**, *516*, 6261–6265.
[70] Y. Wang, Q. Lu, F. Li, D. Guan, Y. Bu, *Adv. Funct. Mater.* **2023**, *33*, 2213523.
[71] a) Q. Shao, P. Wang, X. Huang, *Adv. Funct. Mater.* **2019**, *29*, 1806419; b) P. Wang, K. Jiang, G. Wang, J. Yao, X. Huang, *Angew. Chem. Int. Ed.* **2016**, *55*, 12859–12863; c) D. Zhao, K. Sun, W.-C. Cheong, L. Zheng, C. Zhang, S. Liu, X. Cao, K. Wu, Y. Pan, Z. Zhuang, B. Hu, D. Wang, Q. Peng, C. Chen, Y. Li, *Angew. Chem. Int. Ed.* **2020**, *59*, 8982–8990; d) Y. Wang, L. Chen, X. Yu, Y. Wang, G. Zheng, *Adv. Energy Mater.* **2017**, *7*, 1601390.
[72] G. Zhao, K. Rui, S. X. Dou, W. Sun, *Adv. Funct. Mater.* **2018**, *28*, 1803291.
[73] Y. Dou, Y. Xie, X. Hao, T. Xia, Q. Li, J. Wang, L. Huo, H. Zhao, *Appl. Catal. , B* **2021**, *297*, 120403.
[74] J. Dai, Y. Zhu, H. A. Tahini, Q. Lin, Y. Chen, D. Guan, C. Zhou, Z. Hu, H.-J. Lin, T.-S. Chan, C.-T. Chen, S. C. Smith, H. Wang, W. Zhou, Z. Shao, *Nat. Commun.* **2020**, *11*, 5657.
[75] B. Weng, Z. Song, R. Zhu, Q. Yan, Q. Sun, C. G. Grice, Y. Yan, W.-J. Yin, *Nat. Commun.* **2020**, *11*, 3513.
[76] J. Suntivich, K. J. May, H. A. Gasteiger, J. B. Goodenough, Y. Shao-Horn, *Science* **2011**, *334*, 1383–1385.
[77] a) Z. W. Seh, J. Kibsgaard, C. F. Dickens, I. Chorkendorff, J. K. Nørskov, T. F. Jaramillo, *Science* **2017**, *355*, eaad4998; b) J. H. Montoya, L. C. Seitz, P. Chakthranont, A. Vojvodic, T. F. Jaramillo, J. K. Nørskov, *Nat. Mater.* **2017**, *16*, 70–81; c) A. Vojvodic, J. K. Nørskov, *Science* **2011**, *334*, 1355–1356.
[78] A. Grimaud, O. Diaz-Morales, B. Han, W. T. Hong, Y.-L. Lee, L. Giordano, K. A. Stoerzinger, M. T. M. Koper, Y. Shao-Horn, *Nat. Chem.* **2017**, *9*, 457–465.
[79] C. Jia, X. Xiang, J. Zhang, Z. He, Z. Gong, H. Chen, N. Zhang, X. Wang, S. Zhao, Y. Chen, *Adv. Funct. Mater.* **2023**, *33*, 2301981.
[80] J. B. Goodenough, *Chem. Mater.* **2014**, *26*, 820–829.
[81] a) L. Chong, G. Gao, J. Wen, H. Li, H. Xu, Z. Green, J. D. Sugar, A. J. Kropf, W. Xu, X.-M. Lin, H. Xu, L.-W. Wang, D.-J. Liu, *Science* **2023**, *380*, 609–616; b) H. Liu, Z. Zhang, J. Fang, M. Li, M. G. Sendeku, X. Wang, H. Wu, Y. Li, J. Ge, Z. Zhuang, D. Zhou, Y. Kuang, X. Sun, *Joule* **2023**, *7*, 558–573; c) Z.-Y. Wu, F.-Y. Chen, B. Li, S.-W. Yu, Y. Z. Finfrock, D. M. Meira, Q.-Q. Yan, P. Zhu, M.-X. Chen, T.-W. Song, Z. Yin, H.-W. Liang, S. Zhang, G. Wang, H. Wang, *Nat. Mater.* **2023**, *22*, 100–108.
[82] a) Z. Wang, Y.-R. Zheng, I. Chorkendorff, J. K. Nørskov, *ACS Energy Lett.* **2020**, *5*, 2905–2908; b) Z. Wang, Y.-R. Zheng, J. Montoya, D. Hochfilzer, A. Cao, J. Kibsgaard, I. Chorkendorff, J. K. Nørskov, *ACS Energy Lett.* **2021**, *6*, 2268–2274; c) H. Y. Lin, Z. X. Lou, Y. Ding, X. Li, F. Mao, H. Y. Yuan, P. F. Liu, H. G. Yang, *Small Methods* **2022**, *6*, 2201130; d) Q. Wang, Y. Cheng, H. B. Tao, Y. Liu, X. Ma, D.-S. Li, H. B. Yang, B. Liu, *Angew. Chem. Int. Ed.* **2023**, *62*, e202216645.
[83] D. Liu, X. Li, S. Chen, H. Yan, C. Wang, C. Wu, Y. A. Haleem, S. Duan, J. Lu, B. Ge, P. M. Ajayan, Y. Luo, J. Jiang, L. Song, *Nat. Energy* **2019**, *4*, 512–518.
[84] Q. Shi, C. Zhu, D. Du, Y. Lin, *Chem. Soc. Rev.* **2019**, *48*, 3181–3192.
[85] a) Q. Wang, H. Liu, B. He, J. Qi, D. Wang, H. Xu, N. Zhang, J. Wang, Y. Chen, Z. Wang, Z. Wang, X. Qi, L. Zheng, M. Feng, W. Lü, S. Yan, *Appl. Catal. B: Environ.* **2022**, *317*, 121781; b) L. Yang, K. Zhang, H. Chen, L. Shi, X. Liang, X. Wang, Y. Liu, Q. Feng, M. Liu, X. Zou, *J. Energy Chem.* **2022**, *66*, 619–627.
[86] a) Z. Li, M. Hu, P. Wang, J. Liu, J. Yao, C. Li, *Coord. Chem. Rev.* **2021**, *439*, 213953; b) J. Liu, X. Yang, F. Si, B. Zhao, X. Xi, L. Wang, J. Zhang, X.-Z. Fu, J.-L. Luo, *Nano Energy* **2022**, *103*, 107753.
[87] Y. Li, W. Wang, M. Cheng, Y. Feng, X. Han, Q. Qian, Y. Zhu, G. Zhang, *Adv. Mater.* **2023**, *35*, 2206351.
[88] J. Zhu, Y. Guo, F. Liu, H. Xu, L. Gong, W. Shi, D. Chen, P. Wang, Y. Yang, C. Zhang, J. Wu, J. Luo, S. Mu, *Angew. Chem. Int. Ed.* **2021**, *60*, 12328–12334.
[89] L. Zhao, Z. Tao, M. You, H. Xiao, S. Wang, W. Ma, Y. Huang, B. He, Q. Chen, *Adv. Sci. (Weinh)* **2024**, *11*, 2309750.
[90] W. Zhang, C. Si, Q. Lu, M. Wei, X. Han, S. Chen, E. Guo, *Electrochim. Acta* **2024**, *491*, 144323.
[91] Y.-N. Zhao, C. Liu, S. Xu, S. Min, W. Wang, N. Mitsuzaki, Z. Chen, *Inorg. Chem.* **2023**, *62*, 12590–12599.
[92] J. Junita, D. Jayalakshmi, J. D. Rodney, *Int. J. Hydrog. Energy* **2023**, *48*, 14287–14298.
[93] L. Zhang, H. Jang, Z. Li, H. Liu, M. G. Kim, X. Liu, J. Cho, *Chem. Eng. J.* **2021**, *419*, 129604.
[94] D. Ji, C. Liu, Y. Yao, L. Luo, W. Wang, Z. Chen, *Nanoscale* **2021**, *13*, 9952–9959.
[95] X. Wang, J. Dai, C. Zhou, D. Guan, X. Wu, W. Zhou, Z. Shao, *ACS Mater. Lett.* **2021**, *3*, 1258–1265.
[96] a) J. Zhang, J. Li, C. Zhong, P. Xi, D. Chao, D. Gao, *Nano Lett.* **2021**, *21*, 8166–8174; b) H. Jo, Y. Yang, A. Seong, D. Jeong, J. Kim, S. H. Joo, Y. J. Kim, L. Zhang, Z. Liu, J.-Q. Wang, S. K. Kwak, G. Kim, *J. Mater. Chem. A*

2022, *10*, 2271–2279; c) C. Zhao, N. Li, R. Zhang, Z. Zhu, J. Lin, K. Zhang, C. Zhao, *ACS Appl. Mater. Interfaces* **2019**, *11*, 47858–47867.
[97] a) Y. Liu, X. Liu, X. Wang, H. Ning, T. Yang, J. Yu, A. Kumar, Y. Luo, H. Wang, L. Wang, J. Lee, A. R. Jadhav, H. Hu, M. Wu, M. G. Kim, H. Lee, *ACS Nano* **2021**, *15*, 15017–15026; b) K. Xu, F. Song, J. Gu, X. Xu, Z. Liu, X. Hu, *J. Mater. Chem. A* **2018**, *6*, 14240–14245.
[98] Deeksha, P. Kour, I. Ahmed, Sunny, S. K. Sharma, K. Yadav, Y. K. Mishra, *ChemCatChem* **2023**, *15*, e202300040.
[99] a) C. Liu, D. Ji, H. Shi, Z. Wu, H. Huang, Z. Kang, Z. Chen, *J. Mater. Chem. A* **2022**, *10*, 1336–1342; b) L. Wang, K. A. Stoerzinger, L. Chang, J. Zhao, Y. Li, C. S. Tang, X. Yin, M. E. Bowden, Z. Yang, H. Guo, L. You, R. Guo, J. Wang, K. Ibrahim, J. Chen, A. Rusydi, J. Wang, S. A. Chambers, Y. Du, *Adv. Funct. Mater.* **2018**, *28*, 1803712.
[100] a) Y. Wang, J. Wu, X. Lu, Y. Guo, H. Zhao, X. Tang, *J. Alloys Compd.* **2022**, *920*, 165770; b) D. A. Kuznetsov, J. Peng, L. Giordano, Y. Román-Leshkov, Y. Shao-Horn, *J. Phys. Chem. C* **2020**, *124*, 6562–6570.
[101] M. S. Alom, C. C. W. Kananke-Gamage, F. Ramezanipour, *ACS Omega* **2022**, *7*, 7444–7451.
[102] a) J. Qian, T. Wang, Z. Zhang, Y. Liu, J. Li, D. Gao, *Nano Energy* **2020**, *74*, 104948; b) J.-I. Jung, H. Y. Jeong, J.-S. Lee, M. G. Kim, J. Cho, *Angew. Chem. Int. Ed.* **2014**, *53*, 4582–4586.
[103] N. Kumar, T. Rom, M. Kumar, T. C. Nagaiah, E. Lee, H. C. Ham, S. H. Choi, S. Rayaprol, V. Siruguri, T. K. Mandal, B. J. Kennedy, A. K. Paul, *ACS Appl. Energy Mater.* **2022**, *5*, 11632–11645.
[104] J. Li, L. Zheng, B. Huang, Y. Hu, L. An, Y. Yao, M. Lu, J. Jin, N. Zhang, P. Xi, C.-H. Yan, *Small* **2022**, *18*, 2204723.
[105] a) Q. He, L. Han, C. Lin, K. Tao, *Nanoscale* **2024**, *16*, 12368–12379; b) M. Lu, Y. Zheng, Y. Hu, B. Huang, D. Ji, M. Sun, J. Li, Y. Peng, R. Si, P. Xi, C.-H. Yan, *Sc. Adv.* **2022**, *8*, eabq3563; c) L. Lu, M. Sun, T. Wu, Q. Lu, B. Chen, B. Huang, *Nanoscale Adv.* **2022**, *4*, 680–696.
[106] S. S. Mofarah, E. Adabifiroozjaei, Y. Wang, H. Arandiyan, R. Pardehkhorram, Y. Yao, M. H. N. Assadi, R. Mehmood, W.-F. Chen, C. Tsounis, J. Scott, S. Lim, R. Webster, V. Zhong, Y. Xu, P. Koshy, C. C. Sorrell, *J. Mater. Chem. A* **2020**, *8*, 4753–4763.
[107] W. G. Hardin, J. T. Mefford, D. A. Slanac, B. B. Patel, X. Wang, S. Dai, X. Zhao, R. S. Ruoff, K. P. Johnston, K. J. Stevenson, *Chem. Mater.* **2014**, *26*, 3368–3376.
[108] a) Y. Zhu, W. Zhou, J. Yu, Y. Chen, M. Liu, Z. Shao, *Chem. Mater.* **2016**, *28*, 1691–1697; b) D. Chen, M. Qiao, Y.-R. Lu, L. Hao, D. Liu, C.-L. Dong, Y. Li, S. Wang, *Angew. Chem. Int. Ed.* **2018**, *57*, 8691–8696.
[109] J. Li, F. Yang, Y. Du, M. Jiang, X. Cai, Q. Hu, J. Zhang, *Chem. Eng. J.* **2023**, *451*, 138646.
[110] a) M. E. Kilic, J.-H. Lee, K.-R. Lee, *J. Mater. Chem. A* **2021**, *9*, 13883–13889; b) K. Zhu, F. Shi, X. Zhu, W. Yang, *Nano Energy* **2020**, *73*, 104761.
[111] M. Li, H. Niu, J. Druce, H. Téllez, T. Ishihara, J. A. Kilner, H. Gasparyan, M. J. Pitcher, W. Xu, J. F. Shin, L. M. Daniels, L. A. H. Jones, V. R. Dhanak, D. Hu, M. Zanella, J. B. Claridge, M. J. Rosseinsky, *Adv. Mater.* **2020**, *32*, 1905200.
[112] a) C. Wu, Y. Sun, X. Wen, J.-Y. Zhang, L. Qiao, J. Cheng, K. H. L. Zhang, *J. Energy Chem.* **2023**, *76*, 226–232; b) M. Gong, D.-Y. Wang, C.-C. Chen, B.-J. Hwang, H. Dai, *Nano Research* **2016**, *9*, 28–46; c) J. Wang, S. Mao, Z. Liu, Z. Wei, H. Wang, Y. Chen, Y. Wang, *ACS Appl. Mater. Interfaces* **2017**, *9*, 7139–7147.
[113] J. Wang, C. Cheng, B. Huang, J. Cao, L. Li, Q. Shao, L. Zhang, X. Huang, *Nano Lett.* **2021**, *21*, 980–987.
[114] Y. Qiao, M. Peng, J. Lan, K. Jiang, D. Chen, Y. Tan, *J. Mater. Chem. A* **2023**, *11*, 495–511.
[115] M. Zhang, G. Jeerh, P. Zou, R. Lan, M. Wang, H. Wang, S. Tao, *Mater. Today* **2021**, *49*, 351–377.
[116] a) M. Sun, B. Huang, *Advanced Energy Materials* **2024**, *14*, 2400152; b) Q. Liang, K. Liu, M. Sun, Z. Ren, P. W. K. Fong, J. Huang, M. Qin, Z. Wu, D. Shen, C.-S. Lee, J. Hao, X. Lu, B. Huang, G. Li, *Adv. Mater.* **2022**, *34*, 2200276.

Manuscript received: November 26, 2024
Revised manuscript received: January 5, 2025
Version of record online: February 5, 2025